



NUREG/CR-4439
ORNL/TM-10132

OAK RIDGE
NATIONAL
LABORATORY

MARTIN MARIETTA

LEPRICON Analysis of Pressure Vessel
Surveillance Dosimetry Inserted into
H. B. Robinson-2 during Cycle 9

R. E. Maerker

Prepared for the
U.S. Nuclear Regulatory Commission
Office of Nuclear Regulatory Research
Under Interagency Agreement DOE 40-551-75

OPERATED BY
MARTIN MARIETTA ENERGY SYSTEMS, INC.
FOR THE UNITED STATES
DEPARTMENT OF ENERGY

8610030412 860930
PDR ADOCK 05000261
P PDR

NOTICE

This report was prepared as an account of work sponsored by an agency of the United States Government. Neither the United States Government nor any agency thereof, or any of their employees, makes any warranty, expressed or implied, or assumes any legal liability or responsibility for any third party's use, or the results of such use, of any information, apparatus product or process disclosed in this report, or represents that its use by such third party would not infringe privately owned rights.

Available from

Superintendent of Documents
U.S. Government Printing Office
Post Office Box 37082
Washington, D.C. 20013-7982

and

National Technical Information Service
Springfield, VA 22161

NUREG/CR-4439
ORNL/TM-10132
Distribution Category RL

Engineering Physics and Mathematics Division

**LEPRICON ANALYSIS OF PRESSURE VESSEL SURVEILLANCE DOSIMETRY
INSERTED INTO H. B. ROBINSON-2 DURING CYCLE 9**

R. E. Maerker

NRC Monitor: C. Z. Serpan
Nuclear Regulatory Commission
Washington, DC 20555

Project Manager: F. B. K. Kam
Oak Ridge National Laboratory

Principal Investigator: R. E. Maerker
Oak Ridge National Laboratory

Manuscript Completed: July 28, 1986
Date Published: August 1986

NOTICE This document contains information of a preliminary nature.
It is subject to revision or correction and therefore does not represent a
final report.

Prepared for the
U.S. Nuclear Regulatory Commission
Office of Nuclear Regulatory Research
Under Interagency Agreement DOE 40-551-75
NRC Fin No. B0415

Prepared by the
Oak Ridge National Laboratory
Oak Ridge, Tennessee 37831
operated by
Martin Marietta Energy Systems, Inc.
for the
U.S. DEPARTMENT OF ENERGY
under Contract No. DE-AC05-84OR21400

TABLE OF CONTENTS

Section	Page
I. INTRODUCTION	1
II. CALCULATIONS OF ACTIVITIES AND PRESSURE VESSEL FLUENCES DURING CYCLE 9	5
II.A. Geometry and Materials Description	5
II.B. Source Description	5
II.C. Reference Calculations	9
II.D. Time-Dependent Calculations	11
II.E. Calculated End-of-Cycle Activities and Comparison with Measurements	15
II.F. Calculated End-of-Cycle Critical Pressure Vessel Fluences	17
III. ESTIMATED UNCERTAINTIES IN THE CALCULATED RESULTS	21
IV. ESTIMATED UNCERTAINTIES IN THE MEASUREMENTS	35
IV.A. Random Counting Uncertainties	35
IV.B. Systematic Efficiency Uncertainties	35
IV.C. Bias Factor Uncertainties	37
IV.D. Normalization Uncertainties	37
V. RESULTS OF THE ADJUSTMENT	41
V.A. Adjusted Activities for the Optimum Case	41
V.B. Unfolded Critical Pressure Vessel Fluxes	44
V.C. Adjustments in the Parameters	48
V.D. Adjusted Critical Pressure Vessel Fluences	52
VI. SUMMARY AND CONCLUSIONS	55
ADDENDUM	57
ACKNOWLEDGMENTS	59
REFERENCES	61

LIST OF FIGURES

	Page
Fig. 1. R- θ Octal Section at the Midplane of the HBR-2 Reactor. The location of the maximum fluence in the pressure vessel is along the 0-deg azimuth	3
Fig. 2. Detail of the R- θ Downcomer Dosimetry Capsule Geometry. The dosimeters were located in the immediate vicinity of the cross	6

LIST OF TABLES

Table	Page
I. Midplane Source Normalizations and Other Source Descriptive Data Used in the Analysis of Cycle 9 Dosimetry Measurements	8
II. Some Three-Dimensional Reference Activity Axial Profiles at 0-deg Azimuth on the Inside Surface of the Pressure Vessel	10
III. Three-Dimensional Reference Spectra	12
IV. Reference Saturated Dosimeter Activities	14
V. Comparison of Calculated and Measured End-of-Cycle Activities	16
VI. Comparison of Calculated and Measured Axial Profiles of End-of-Cycle Activities at 0 deg in the Cavity	18
VII. Comparison of Calculated and Measured Axial Profiles of End-of-Cycle Activities at 12 deg in the Cavity	19
VIII. Fluences Accumulated During Cycle 9 for Two Critical Pressure Vessel Locations	20
IX. Flux Bias Factors Assumed in the Calculations and Their Correlations	23
X. Standard Deviations in the Fluxes at the Downcomer Dosimeter Location Arising from Parameter Uncertainties	24
XI. Standard Deviations in the Fluxes at the Cavity Dosimeter Location Arising from Parameter Uncertainties	25
XII. Standard Deviations in the Fluxes at the Critical LCW and T/4 Pressure Vessel Locations Arising from Parameter Uncertainties	26
XIII. Autocorrelation Matrix of the Calculated Group Fluxes at the Downcomer Dosimetry Location	28
XIV. Autocorrelation Matrix of the Calculated Group Fluxes at the Cavity Dosimetry Location	29
XV. Autocorrelation Matrix of the Calculated Group Fluxes at the Critical LCW Pressure Vessel Location	30
XVI. Autocorrelation Matrix of the Calculated Group Fluxes at the Critical T/4 Pressure Vessel Location	31

LIST OF TABLES (cont'd)

Table	Page
XVII. Complete Correlation Matrix of the Calculated Activities	32
XXVIII. Cross-Correlation Matrix Between the Calculated Critical Pressure Vessel Fluxes and the Dosimeter Activities	33
XIX. Gamma Rays Counted for Each Reaction and Assumed Efficiency Energy Correlations	36
XX. Complete Correlation Matrix of the Measured Activities	39
XXI. Comparison of Calculated (C) and Adjusted (A) HBR-2 Activities with Measurement (E)	42
XXII. Complete Correlation Matrix of the Adjusted Activities	43
XXIII. Flux Adjustments and Standard Deviations at the Critical LCW Pressure Vessel Location as Functions of the HBR-2 Measurements Activated	45
XXIV. Flux Adjustments and Standard Deviations at the Critical T/4 Pressure Vessel Location as Functions of the HBR-2 Measurements Activated	46
XXV. Autocorrelation Matrix of the Adjusted Group Fluxes at the Critical LCW Pressure Vessel Location	47
XXVI. Autocorrelation Matrix of the Adjusted Group Fluxes at the Cavity Dosimetry Location	49
XXVII. Summary of Present and Past Adjustments in the Total Inelastic Cross Section of Iron in the 3- to 8-MeV Region	50
XXVIII. Adjustments and Standard Deviations in the Pressure Vessel Out-of-Roundness Bias Factor at the Cavity Dosimeter and Critical Pressure Vessel Locations	51
XXIX. Adjusted Group Fluences at the Critical Pressure Vessel Locations Accumulated During Cycle 9	53
XXX. Weighted Fluences at the Critical Pressure Vessel Locations Accumulated During Cycle 9 with Standard Deviations Before and After Unfolding	54
XXXI. Comparisons with Measurement of Calculated End-of-Cycle Activities Using Original and Updated Iron Cross Sections	58

ABSTRACT

A second example of applying the LEPRICON methodology to an existing pressurized water reactor is described. The present application is an analysis of ad hoc dosimetry inserted into the H. B. Robinson-2 reactor to monitor the effects on pressure vessel fluence produced by the introduction of a low-leakage fuel management scheme during cycle 9. The use of simultaneous dosimetry both at a downcomer location and in the reactor cavity allowed a quantitative evaluation to be made by the LEPRICON procedure of the relative merits of each location. Unfolded results using the dosimetry indicate that the cumulative neutron fluence above 1 MeV originally calculated for the critical lower circumferential weld in the pressure vessel during cycle 9, $7.2 \times 10^{17} \text{ n/cm}^2 \pm 15.9$ percent, should be adjusted upward by about one standard deviation to a value of $8.4 \times 10^{17} \text{ n/cm}^2$ with a reduced uncertainty of 10.9 percent.

EXECUTIVE SUMMARY

It has been demonstrated that the LEPRICON computer code system, as it now exists, can be successfully applied to the analysis of surveillance dosimetry recently installed in an older Westinghouse three-loop reactor. Since the reactor design as well as in-core instrumentation analysis procedures for the HBR-2 reactor and the Arkansas Nuclear One-Unit 1 (ANO-1) reactor analyzed earlier are different, it is comforting to know that the code system is sufficiently general to be able to treat geometries of considerable diversity, as well as being capable of taking advantage of core-follow analysis routinely performed by different vendors such as Westinghouse and Babcock and Wilcox.

At the beginning of the present analysis, it was felt that the presence of the relatively narrow reactor cavity in HBR-2 might introduce calculational problems that were absent in the wide cavity of ANO-1. Such was not the case, however, either because the cavity was not so narrow as to cause a streaming problem over the range of heights investigated, the presence of two deep and wide detector wells effectively widened the cavity, or the core source distribution was flat over much of the axial range analyzed, or perhaps a combination of all three. For whatever reason, no progress could be made on refining the knowledge of the bias factor arising from streaming effects on off-midplane dosimetry locations in narrow cavities that is included as a parameter in the LEPRICON system and which could still apply to certain other reactors.

The considerably off-midplane location of the lower circumferential weld was also somewhat of a preanalysis worry, since the axial range of validity of the three-dimensional flux synthesis procedure was not severely tested in ANO-1. Fortunately, in HBR-2 the axial flatness of the source beyond this point ensured the success of the procedure.

There still exist reactors, however, for which a priori values for the flux synthesis bias factors are not unity, i.e., reactors in which the locations of critical pressurized thermal shock (PTS)-sensitive welds fall beyond the range of validity of the simple synthesis procedure. Such axial locations occur in regions of large vertical flux gradients occasioned by proximity to the limits of the active core and beyond. Evaluation of these bias factors still needs to be performed before the LEPRICON procedure can be applied indiscriminately to end-of-life and PTS pressure vessel locations alike.

The results of the present analysis are similar to those from ANO-1. Meaningful reductions in the estimated standard deviations of the pressure vessel fluences accumulated during cycle 9 from 16 to 11 percent were obtained for both locations, with the adjusted fluences being about 15 percent higher. By eliminating one of the 12 measurements, the HBR-2 data were found to be consistent with previously analyzed benchmark data that form an important part of the data base developed for the adjustment procedure.

Of the two dosimetry locations simultaneously employed in HBR-2, those in the cavity offer more information on the pressure vessel fluxes because they have about the same sensitivity to any pressure vessel out-of-roundness as either critical pressure vessel location; they also possess high sensitivity to inaccuracies in the steel transport cross sections which also affect the pressure vessel fluxes.

LEPRICON ANALYSIS OF PRESSURE VESSEL SURVEILLANCE DOSIMETRY
INSERTED INTO H. B. ROBINSON-2 DURING CYCLE 9

I. INTRODUCTION

The theory of the generalized linear least-squares combination procedure used in the LEPRICON adjustment module of the LEPRICON computer code system¹ and the application of the procedure to pressure vessel surveillance dosimetry were described in an earlier publication.² Also described was the development of a dosimetry benchmark data base that could be used in the combination procedure to permit a simultaneous adjustment of the benchmark data with measurements performed in a pressurized water reactor (PWR).

A second paper³ described the extension of the LEPRICON code system to include additional modules which provide standard methods for calculating a priori pressure vessel fluence and dosimeter activity estimates with transport theory using the method of discrete ordinates. Results of an application using portions of this expanded LEPRICON system to measurements performed in the cavity of the Arkansas Nuclear One-Unit 1 reactor (ANO-1) were also presented in great detail.

Among the methods introduced in this generalized LEPRICON code system are procedures for incorporating the results of core physics calculations with in-core measurements to provide sources for the transport codes. Another technique involves the use of a single adjoint function in conjunction with the results of a forward transport calculation to obtain accurate estimates of the effects of time-dependent source spatial distributions on dosimeter activities and pressure vessel fluences. These procedures were described in a third paper.⁴

The purpose of this paper is to present the results of a second application of the LEPRICON system to an on-line PWR, this time using the complete set of modules which are in the process of being fully documented by the Electric Power Research Institute (EPRI), thus supplementing the earlier experience with ANO-1, a Babcock and Wilcox designed reactor. This new application is to the H. B. Robinson-2 reactor (HBR-2), a 2300-MW (thermal) PWR designed by Westinghouse (W) and placed in operation in March of 1971. This three-loop reactor is representative of an older class of W reactors which are further characterized by a relatively narrow 170.7-mm (6.72-in.) annular reactor cavity. Conventional dosimetry (i.e., sequential extraction of downcomer-positioned surveillance capsules only) had been utilized over the first eight cycles of reactor operation. Increasing concern regarding the possible rupture of the lower circumferential weld (LCW) in the pressure vessel due to pressurized thermal shock (PTS) following a loss of coolant accident resulted in the adoption of two measures designed to reduce the subsequent accumulation of fluence at this and other locations.

The first measure, introduced at the beginning of cycle 9, involved a change in the fuel loading pattern. Instead of being removed, previously burned fuel was placed in the outermost row of the core in the assemblies defining the flats at 0-deg azimuth (see Fig. 1). (The remaining peripheral assemblies were still replaced with fresh fuel, however.) This azimuth, as well as those at 90 deg, 180 deg and 270 deg, defines the location of maximum fluence rate in the pressure vessel (see Section II) and hence is the azimuth at which the fluence accumulated at the lower circumferential weld, located 1150 mm (3.77 ft) below the reactor midplane, is considered to be of critical importance. Previous calculations had indicated about a factor of two reduction in the fluence rate at this critical weld location effected by the revised fuel management scheme.⁵ The second fluence-reducing measure was not introduced until cycle 10, when it was used in concert with the low-leakage core; therefore, it will not be considered here, but interested readers can refer to Ref. 5. for further information.

In order to validate the calculated effectiveness of the low-leakage core, special dosimetry was introduced during cycle 9 at several locations. A surveillance capsule containing no metallurgical specimens but otherwise identical to a standard W capsule (the region which normally contained the specimens was filled with carbon steel) was placed at the 20-deg azimuth location in the downcomer as indicated in Fig. 1. The capsule was firmly attached to the rear of the thermal shield and contained dosimetry that included six threshold reactions, as well as several other foils that involved low-energy responses which were not analyzed with LEPRICON. Dosimetry using the same threshold reactions was also simultaneously inserted into the reactor cavity at 0-deg azimuth (see Fig. 1) by means of a thin aluminum holder that can be assumed to be transparent to neutrons. The holder was attached to a stainless steel wire that itself was secured near the top and bottom of the cavity. Both the downcomer dosimetry and the 0-deg cavity dosimetry were located in the reactor midplane and constituted the measurements to be analyzed in the LEPRICON adjustment procedure.

Supplementing these 12 threshold dosimetry measurements were several ^{54}Mn activity measurements from the $^{54}\text{Fe}(n,p)$ reaction in the cavity above and below the midplane at 0 deg and on the midplane at 12, 30, and 42 deg. Except for the 42-deg location (not shown in Fig. 1 and not analyzed by LEPRICON), all the aforementioned measurements were located in the same octant. All these dosimeter measurements were performed by Hanford Engineering Development Laboratory.

A final series of measurements, performed by Westinghouse, involved counting 304.8-mm (1-ft) sections of the steel wires themselves, for each of the four azimuthal cavity locations, to determine ^{54}Mn , ^{58}Co , and ^{60}Co activities arising from the $^{54}\text{Fe}(n,p)$, $^{58}\text{Ni}(n,p)$, and $^{59}\text{Co}(n,\gamma)$ reactions respectively, in the stainless steel. These latter measurements provided axial profiles in the cavity that ranged from above to below the active core.

In Section II a description of the calculations of the dosimeter activities and pressure vessel fluences during cycle 9 is presented using the various transport-oriented modules that are included in the LEPRICON

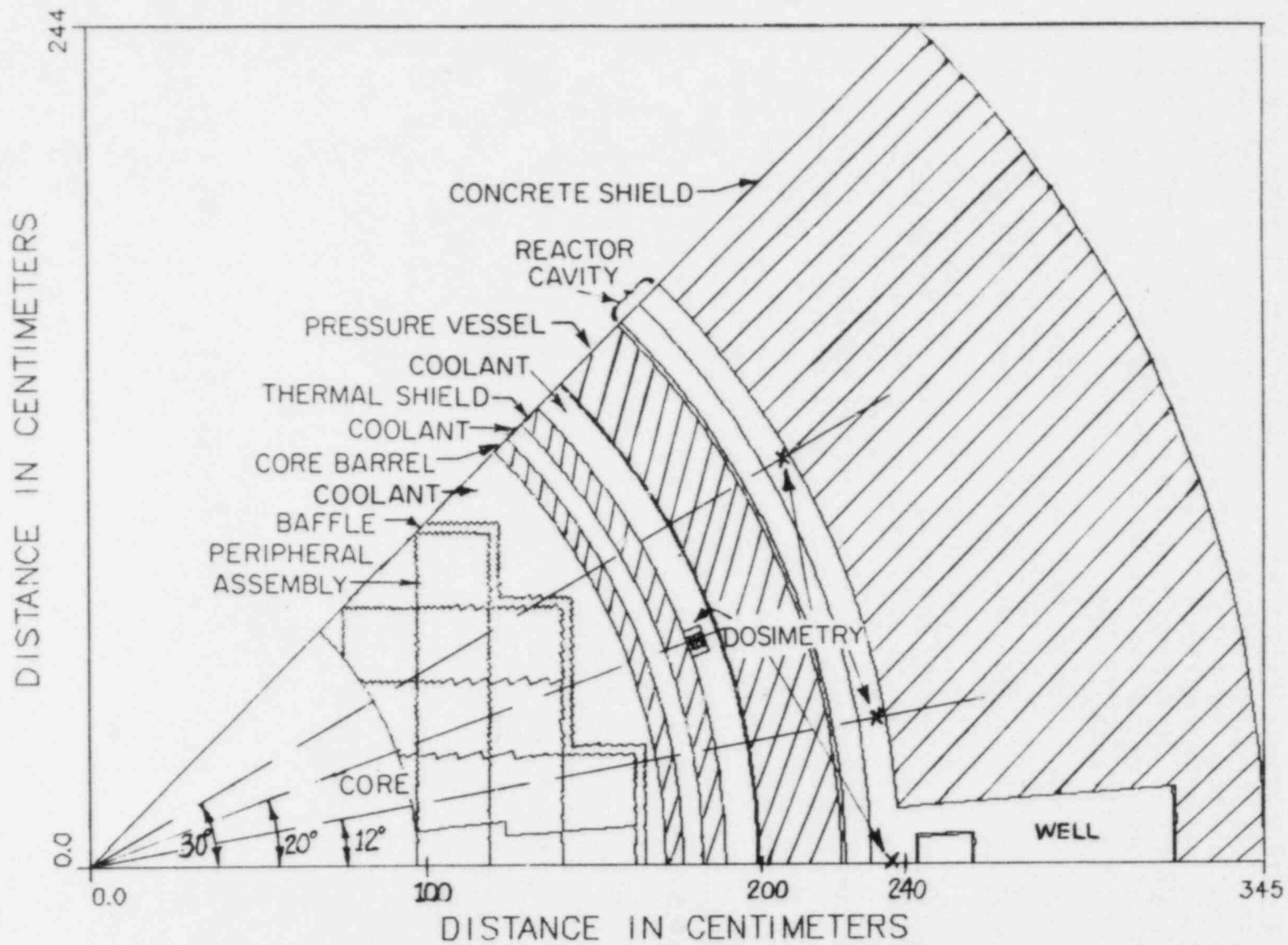


Fig. 1. R- θ Octal Section at the Midplane of the HBR-2 Reactor. The location of the maximum fluence in the pressure vessel is along the zero-degree azimuth.

code system, and comparisons with the measurements are made. This section can also serve as a further clarification of the sequence of calculations involved in using the various modules of the LEPRICON system.

A discussion of the estimated uncertainties in the 12 calculated dosimeter activities and pressure vessel group fluences at the two locations that are to be input into the LEPRICON combination procedure appears in Section III. This section also discusses the choice of bias factors applicable to the HBR-2 calculations and presents the contribution to the overall uncertainties of the calculated quantities arising from uncertainties in these bias factors.

A brief presentation of the estimated covariances of the 12 dosimeter measurements appears in Section IV, following the guidelines introduced in an analysis of similar ANO-1 measurements presented in Ref. 3.

The major results from the LEPRICON adjustment procedure are detailed in Section V, where comparisons between á priori and á posteriori activities and pressure vessel group fluences may be made along with their corresponding covariances. Effects of varying the number of HBR-2 measurements that enter into the adjustment procedure are also investigated, and indeed, eliminating one of the 12 measurements was found to be indicated. The relative merits of downcomer vs. cavity dosimetry are quantitatively examined. Finally, several weighted fluences (i.e., fluence above 1 MeV, fluence above 0.1 MeV, and displacements per atom) at two pressure vessel locations and their standard deviations are presented for cycle 9 for conditions similar to those described above for the group fluences.

A summary of the conclusions that may be drawn from this further application of the complete LEPRICON methodology to a reactor of considerably different design from the first one, as well as one for which the time sequence and location of the dosimetry are also quite different, appears in Section VI.

II. CALCULATIONS OF ACTIVITIES AND PRESSURE VESSEL FLUENCES DURING CYCLE 9

II.A. Geometry and Materials Description

An octal section of a plan view through the horizontal midplane of the HBR-2 reactor to beyond the biological shield is shown in Fig. 1 in the form of a plot of the R- θ variable mesh geometry employed in the transport calculations. This geometry required 74 azimuthal intervals and between 93 and 112 radial intervals for each azimuthal interval. The dummy surveillance capsule containing the downcomer dosimetry that is indicated in Fig. 1 is shown in more detail in Fig. 2. The cavity dosimetry locations are indicated in Fig. 1 by crosses for those measurements investigated in the present analysis. The reactor cavity region immediately behind the 241.55-mm thick (9.51-in.) pressure vessel [the first 5.56 mm (0.219 in.) of which consists of a stainless steel liner] is composed of a 12.7-mm (0.5-in.) air gap followed by a 76.2-mm (3-in.) insulation region containing iron at 3 percent normal density followed by another 81.79-mm (3.22-in.) air gap. There are two relatively wide (~ 6.83 -deg) and deep (~ 806 -mm or 31.75-in.) detector wells that replace much of the concrete backing the cavity at 0 and 45 deg (only the one at 0 degrees was approximated in the R- θ geometry and is pictured), with a 190.5-mm-OD (7.5-in.) iron cylinder, 6.35 mm (0.25 in.) thick, placed inside each well. Since the cavity is relatively narrow [as contrasted with the 1067-mm-wide (3.5-ft) cavity in ANO-1], any difficulty that might otherwise have been experienced in calculating axial streaming throughout this region is probably alleviated by the presence of these detector wells (see comparison of measured and calculated axial cavity profiles presented later in this section). The concrete composition was assumed to be that of type 02-b ordinary concrete⁶ with two changes: the water content was reduced to 4.67 percent by weight⁷ and the iron concentration was increased to reflect an estimated 0.7 percent by volume⁸ addition of rebar. No steel liner covered the cavity concrete wall, but there was a 6.35 mm-thick (0.25-in.) liner that covered all concrete surfaces in the detector well.

Cycle 9 was run at somewhat cooler temperatures than those of the earlier cycles, which resulted in somewhat higher coolant densities. The coolant densities were in the vicinity of 0.766 g/cm³ and 0.789 g/cm³ for the fuel region and all ex-baffle regions respectively.

The assumed axial geometry consisted of an active fuel region 3660 mm (12 ft) high, an inactive fuel region followed by a second region consisting of steel and coolant, both above the core, and a steel and coolant region below the core.⁹

II.B. Source Description

The three-dimensional source distributions as a function of time throughout cycle 9 were determined in a fashion consistent with the source

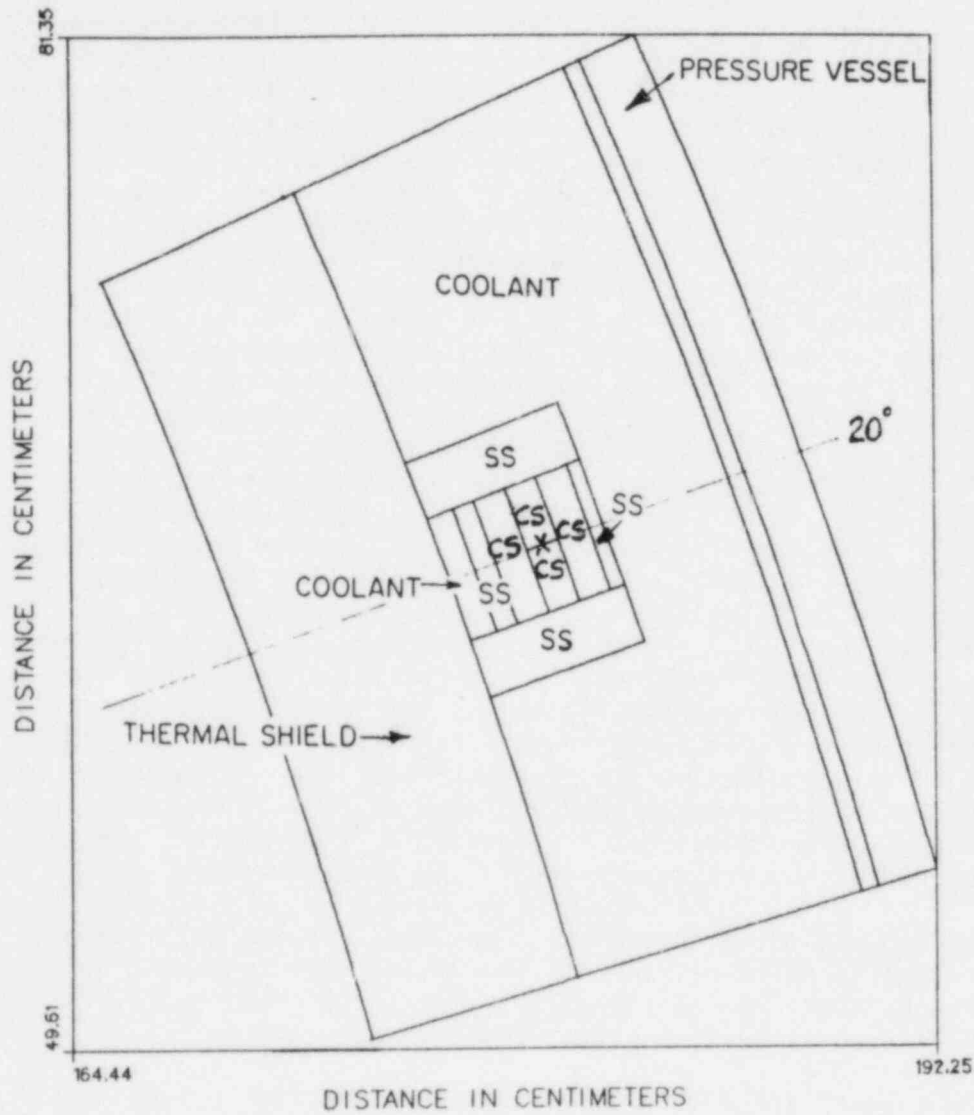


Fig. 2. Detail of the R- θ Downcomer Dosimetry Capsule Geometry. The dosimeters were located in the immediate vicinity of the cross.

preparation module DOTSOR^a in the LEPRICON system. Through the cooperation of W. K. Cantrell and S. P. Grant of Carolina Power and Light (CP&L), measured data processed by the Westinghouse INCORE program were made available which provided instantaneous assembly power information at various axial levels throughout the core for several different times during the cycle. Data in the form of card images representing pin power distributions calculated by PDQ7 were also supplied at approximately the same cycle exposure increments as those represented by the above INCORE results. Fission neutron source data for the midplane R- θ transport calculations were then obtained by normalizing the pin power data to the axially integrated INCORE powers for each peripheral assembly and using an exposure-dependent conversion factor typical of the multiply burned peripheral assemblies at 0-deg azimuth to relate source strength to power level.^a Fission spectra were also used that were intermediate between the ENDF/B-V values of the fission spectra for ²³⁵U and ²³⁹Pu. There were in all eight of these absolute midplane source distributions determined at roughly equal exposure increments throughout the cycle.

Daily averages of the reactor power operating levels and accumulated exposures were also furnished by CP&L for cycle 9 to permit correlations to be made between the eight spatial source distributions and the coarse time intervals over which the source data were assumed to be representative, as well as to provide a detailed power history on a fine enough scale that the end-of-cycle dosimeter activities and accumulated pressure vessel fluences could be accurately calculated.

A summary of the various midplane source normalizations and other source descriptive data is shown in Table I. The exposure values are cumulative but the effective full power days (EFPD) appearing in the last column are not. The entries in the next-to-the-last column reflect the fact that the core leakage increases during the cycle (i.e., the power distribution is shifting outward), in contrast to the situation for ANO-1 described in Ref. 3 in which the low-leakage core during cycles 4 and 5 displayed very little in-cycle variations of any kind.

The changes in the relative axial distributions during cycle 9 for all peripheral assemblies, as indicated by the INCORE data, were small. The effect was a slight further flattening of an already rather flat distribution. For axial locations lying within about 1400 mm (4.6 ft) of the midplane, the local variation during cycle 9 burnup was about 10 percent or less, and the distribution at any instant was also flat to within about 10 percent. Consequently the midcycle distribution characteristic of the 0-deg assemblies assumed as the reference source for the R-Z transport calculation is considered to be more than adequately representative of the entire cycle.

^aReferences 3 and 4 provide descriptions of this source preparation procedure.

Table I. Midplane Source Normalizations and Other Source Descriptive Data Used in the Analysis of Cycle 9 Dosimetry Measurements

Source Data	Power [MW(thermal)]	Date Recorded	Incore Cycle 9 Exposure (MWD/MTU) ^a	PDQ7 Cycle 9 Exposure (MWD/MTU) ^a	Assumed Time Interval Represented	Days ^b	Iron Activity [cm x rps/atom x MW(thermal) ⁻¹] ^c	Effective Full Power Days Duration (EFPD)	
Start: 8/21/82									
1	1814.2	9/1/82	180	100	8/21-9/6	17	2.60-18 ^d	8.80	
2	1734.7	9/16/82	417	500	9/7-10/8	32	2.60-18	20.75	
3	1809.0	11/2/82	1632	1500	10/9-12/5	58	2.86-18	44.72	
4	1777.7	1/11/83	3363	3500	12/6-2/23	80	3.18-18	59.23	∞
5	1782.9	3/31/83	5445	5500	2/24-6/15	112	3.65-18	58.94	
6	1761.4	7/26/83	7595	7500	6/16-8/31	77	3.97-18	58.89	
7	990.2	12/19/83	9890	9500	9/1-12/25	116	4.08-18	43.67	
8	1254.4	1/12/84	10379	10500	12/26-1/26	32	4.07-18	18.81	
End: 1/26/84 at 10637 MWD/MTU and 313.81 EFPD									

^aMWD/MTU = megawatt days per metric ton of uranium.

^bIncluding down time, of which there were 0, 3, 2, 1, 30, 0, 49, and 0 full days in the eight time intervals respectively. The daily load factor averaged over the duration of 524 calendar days was 0.599; excluding full-day down time, the load factor averaged 0.715.

^cAxially integrated saturated activity of the $^{54}\text{Fe}(n,p)^{54}\text{Mn}$ reaction on the midplane at 0-deg azimuth in the cavity (i.e., at the location of the six cavity dosimeter measurements).

^dRead as 2.60×10^{-18} .

II.C. Reference Calculations

Three reference transport calculations using the ELXSIR cross-section library¹⁰ were performed - one each in R- θ , R-Z, and R geometries. The axially integrated source for the R- θ calculation was taken to be the one compounded from INCORE and PDQ7 data near midcycle, which in this case was chosen to be the source data listed in the fifth row of Table I. The DOTSOR module was used to prepare not only the R- θ reference source but also the remaining distributions in Table I as well, employing the same R- θ variable mesh that describes the geometric input to the DOT4 transport code. The same module also was used to prepare the reference azimuthally integrated R-Z source in the same fixed mesh consisting of 89 radial and 75 axial intervals employed in the R-Z DOT4 transport calculation. The ex-core R-Z mesh described the geometry at zero degrees azimuth since this is the direction of greatest interest. The DOTSOR module also prepared the reference R source, obtained by integrating the reference R-Z source over Z, in the same radial mesh as the R-Z, for use in a one-dimensional ANISN transport calculation. The results from each of these three reference calculations, using the ELXSIR cross-section library developed as part of the LEPRICON system, were then combined in a flux synthesis procedure³ to yield three-dimensional reference fluxes throughout the reactor geometry using the DOTSYN module of the LEPRICON system.

The azimuthal profile at one-quarter depth into the pressure vessel (referred to as a T/4 location) using the results of the reference R- θ calculation indicates that there is very close to a threefold decrease in the flux above 1 MeV at 45 deg compared to the flux above 1 MeV at 0 deg. Thus, although the azimuth of maximum flux remains 0 deg, the substitution of multiply burned fuel for fresh fuel in the peripheral assemblies near 0 deg in cycle 9 has decreased the flux in the vicinity of the major core axis by about a factor of two over that of earlier cycles, in which the flux ratio between 0 and 45 deg was close to a factor of six.⁵ The situation in the cavity is complicated by the presence of the detector wells at 0 and 45 deg, since only one well was modelled in the calculation and the effect of the well on the midplane cavity fluxes may be important because it does not provide a strong reflected local component back into the detector. The cavity measurements indicate about a factor of six decrease in the ⁵⁴Mn activity at 42 deg relative to that at 0 deg, which would seem to indicate a changing azimuthal profile between the T/4 and cavity locations.

Some axial activity profiles at 0-deg azimuth in the stainless steel liner on the inside of the pressure vessel determined from the flux synthesis of the three reference calculations are shown in Table II. The spectrum is seen to be virtually independent of height, and the axial profiles are very similar to that of the source. The critical location of the LCW (on the inner surface of the pressure vessel at 0-deg azimuth and about 118 cm below the midplane) is seen to lie within the flat part of the profile, so that little error should be introduced in using the flux synthesis procedure at this off-midplane location.

Table II. Some Three-Dimensional Reference Activity Axial Profiles at 0-deg Azimuth on the Inside Surface of the Pressure Vessel

Distance Above Midplane (cm)	Saturated Activities (rps/atom)			Weighted Fluxes ($n \cdot s^{-1} cm^{-2}$)	
	$^{63}Cu(n, \alpha)$	$^{54}Fe(n, p)$	$^{237}Np(n, f)$	$\phi > 1 MeV$	$\phi > 0.1 MeV$
207	1.96-18 ^a	1.58-16	3.51-15	1.43+9	4.07+9
199	3.02-18	2.57-16	6.03-15	2.45+9	7.04+9
192	4.46-18	3.97-16	9.57-15	3.90+9	1.11+10
184 ^b	6.32-18	5.81-16	1.42-14	5.81+9	1.63+10
170	1.03-17	9.70-16	2.40-14	9.87+9	2.73+10
137 ^c	1.82-17	1.72-15	4.27-14	1.76+10	4.81+10
107	2.14-17	2.01-15	4.98-14	2.05+10	5.63+10
76	2.21-17	2.08-15	5.13-14	2.11+10	5.82+10
46	2.26-17	2.12-15	5.25-14	2.16+10	5.95+10
0	2.29-17	2.16-15	5.34-14	2.19+10	6.04+10
-46	2.31-17	2.18-15	5.38-14	2.21+10	6.09+10
-78	2.33-17	2.19-15	5.42-14	2.23+10	6.14+10
-118 ^d	2.24-17	2.11-15	5.23-14	2.15+10	5.91+10
-137 ^c	2.07-17	1.96-15	4.87-14	2.00+10	5.49+10
-170	1.29-17	1.22-15	3.02-14	1.25+10	3.40+10
-190 ^b	5.73-18	5.08-16	1.18-14	4.90+9	1.30+10

^aRead as 1.96×10^{-18} .

^bApproximate limits of the active core.

^cApproximate limits defining the flat axial profile region of the source.

^dApproximate location of the lower circumferential weld.

The reference synthesized flux spectra down to 0.1 MeV in the ELXSIR group structure at five important locations are shown in Table III. In this as well as all succeeding tables, the critical T/4 location is at the position of maximum flux (0-deg azimuth and about 78cm below the midplane). The flatness of the source axial profile renders the fluxes at the inner pressure vessel surface near the midplane (indicated as OT) and the LCW locations virtually identical. The saturated reference activities corresponding to the conditions leading to the fluxes in Table III [midcycle source distribution at a power of 1782.9 MW (thermal)] appear in Table IV. Comparison of the activities at the two dosimetry locations shows that they differ by factors of about 130 for the higher threshold reactions and by a factor of about 20 for the Np reaction, which has the lowest threshold in the vicinity of 0.1 MeV. Effects of axial leakage produced by the finite core height are virtually negligible in HBR-2. Leakage factors are virtually unity for all group fluxes at the downcomer dosimetry and pressure vessel locations, and they lie between 0.92 and 0.98 for the six dosimeter responses located in the cavity.

II.D. Time-Dependent Calculations

The procedures described in Refs. 3 and 4 were followed to incorporate the effects of time dependence of the source spatial distribution into the LEPRICON methodology by using an appropriately chosen adjoint function calculated with the same R- θ geometry employed in the forward calculation with the reference source. As suggested in Ref. 3, the $^{54}\text{Fe}(n,p)^{54}\text{Mn}$ reaction cross section was used to generate the adjoint function, with the adjoint source being placed at the location of the 0-deg cavity dosimetry. The resulting adjoint fluxes were then folded with the reference R- θ source in a steady-state calculation using the TIMEPATCH module, another part of the LEPRICON system, and the forward- and adjoint-calculated saturated activities for the $^{54}\text{Fe}(n,p)$ reaction were compared. The agreement was very good and established a small correction factor of 1.0074 which could be used in the future to convert all adjoint-calculated quantities in HBR-2 to equivalent forward-calculated values. By means of the adjoint-scaling technique introduced and discussed in Refs. 3 and 4, pressure vessel group fluences and all dosimeter end-of-cycle activities were obtained by folding the adjoint function with each of the eight midplane sources calculated with DOTSOR in turn and superimposing the power history in accordance with the time correlations indicated in Table I. The adjoint scaling of the quantities determined from the forward reference calculations and the effects of power level variations on the accumulated pressure vessel fluences and activities at the end of cycle were all accomplished using the time-dependent option of the TIMEPATCH module.

Before proceeding further, an additional comparison was made to test the accuracy of the adjoint-scaling technique in HBR-2 when applied to the two far-removed dosimeter locations. Implicit in the adjoint-scaling technique for estimating a response at a new location by using an adjoint function based on perhaps another response at another location is the assumption that the sensitivities to the various assembly sources of the

Table III. Three-Dimensional Reference Spectra

Group	Lower Energy (MeV)	Flux ($n \cdot s^{-1} cm^{-2}$)				
		20° Downcomer	0° Cavity	LCW	OT ^a	T/4 ^b
1	14.2	4.06+6 ^C	4.94+4	3.55+6	3.69+6	1.40+6
2	12.2	2.05+7	2.71+5	1.77+7	1.83+7	7.11+6
3	11.1	2.64+7	3.22+5	2.27+7	2.36+7	9.01+6
4	10.0	5.94+7	6.66+5	5.13+7	5.32+7	2.01+7
5	8.61	1.76+8	1.79+6	1.51+8	1.56+8	5.84+7
6	8.19	8.25+7	7.84+5	7.07+7	7.31+7	2.71+7
7	7.41	2.25+8	1.91+6	1.96+8	2.03+8	7.30+7
8	7.05	1.27+8	1.05+6	1.10+8	1.14+8	4.12+7
9	6.07	5.97+8	4.21+6	5.33+8	5.50+8	1.90+8
10	4.97	1.00+9	6.14+6	9.08+8	9.37+8	3.11+8
11	4.07	1.24+9	7.34+6	1.13+9	1.17+9	3.87+8
12	3.68	6.12+8	3.84+6	5.36+8	5.52+8	1.91+8
13	3.01	1.57+9	1.13+7	1.33+9	1.37+9	5.01+8
14	2.73	1.26+9	1.03+7	1.04+9	1.07+9	4.26+8
15	2.59	7.57+8	7.02+6	6.08+8	6.26+8	2.65+8
16	2.47	7.22+8	6.05+6	6.10+8	6.28+8	2.53+8
17	2.37	7.40+8	6.85+6	6.23+8	6.41+8	2.67+8
18	2.35	2.25+8	2.58+6	1.78+8	1.83+8	8.25+7
19	2.23	1.08+9	1.30+7	8.31+8	8.55+8	4.04+8
20	2.12	9.43+8	1.07+7	7.21+8	7.42+8	3.55+8
21	1.92	1.77+9	1.99+7	1.36+9	1.39+9	6.73+8
22	1.83	1.00+9	1.42+7	6.87+8	7.06+8	3.87+8

Table III (Continued)

Group	Lower Energy (MeV)	Flux ($n \cdot s^{-1} cm^{-2}$)				
		20° Downcomer	0° Cavity	LCW	OT ^a	T/4 ^b
23	1.65	2.38+9	4.15+7	1.63+9	1.67+9	9.38+8
24	1.50	2.19+9	3.67+7	1.54+9	1.58+9	8.86+8
25	1.35	2.63+9	5.42+7	1.71+9	1.75+9	1.08+9
26	1.23	2.59+9	5.65+7	1.61+9	1.65+9	1.05+9
27	1.00	6.37+9	2.11+8	3.46+9	3.56+9	2.66+9
28	0.907	3.10+9	1.51+8	1.63+9	1.68+9	1.42+9
29	0.821	3.37+9	1.65+8	1.78+9	1.83+9	1.43+9
30	0.743	3.06+9	1.29+8	1.82+9	1.87+9	1.29+9
31	0.608	8.80+9	8.91+8	5.20+9	5.37+9	5.71+9
32	0.498	7.21+9	6.54+8	4.11+9	4.24+9	3.99+9
33	0.369	7.83+9	8.48+8	5.14+9	5.30+9	5.81+9
34	0.302	6.72+9	1.21+9	4.40+9	4.56+9	5.42+9
35	0.213	8.13+9	1.15+9	5.13+9	5.30+9	5.26+9
36	0.183	2.72+9	3.36+8	1.83+9	1.89+9	1.78+9
37	0.111	9.29+9	1.23+9	5.79+9	5.99+9	5.76+9
38	0.098	1.52+9	1.93+8	1.03+9	1.07+9	9.10+8

^aInside surface of the pressure vessel at the location of maximum flux, which is at 0-deg azimuth and about 78 cm below the midplane (see Table II).

^bAt one-quarter thickness into the pressure vessel at the same location of maximum flux as above.

^cRead as 4.06×10^6 .

Table IV. Reference Saturated Dosimeter Activities

Location	Activities in reactions/sec per target atom					
	$^{63}\text{Cu}(n,\alpha)$	$^{46}\text{Ti}(n,p)$	$^{54}\text{Fe}(n,p)$	$^{58}\text{Ni}(n,p)$	$^{238}\text{U}(n,f)$	$^{237}\text{Np}(n,f)$
20° Downcomer	2.57-17 ^a	4.07-16	2.45-15	3.26-15	1.11-14	7.91-14
0° Cavity	2.24-19	3.12-18	1.88-17	2.72-17	1.37-16	3.39-15

^aRead as 2.57×10^{-17} .

responses at the two locations are similar. As has been pointed out earlier, for HBR-2 there is a three- to six-fold flux variation over the azimuthal range from 0 to 45 deg, thus indicating significantly different sensitivities to the various assembly sources for detectors located at different azimuths. In particular, there exists the possibility of introducing a significant error in the present adjoint-scaling procedure when estimating the activities at 20 deg in the downcomer region using an adjoint function based on a 0-deg location in the cavity. This error was quantified by performing a second forward R- θ transport calculation using as a source the end-of-cycle distribution which appears as the last row in Table I. The activities calculated by adjoint scaling of the reference source can now be compared with those from the second forward calculation. The ratio of the R- θ adjoint-calculated $^{54}\text{Fe}(n,p)$ saturated activities in the cavity obtained by folding first source No. 8 in Table I with the adjoint function and then the reference source (No. 5) with the same adjoint function is 0.785. Comparison of the values obtained by multiplying the fluxes from the reference forward R- θ calculation by 0.785 with those from the second forward calculation using the end-of-cycle source shows that all group fluxes lying above 0.1 MeV are accurate to within ± 0.5 percent at the cavity detector and ± 1.0 percent at the critical LCW and T/4 locations, all 0-deg azimuth locations, and to within 6.6 ± 0.6 percent at the 20-deg downcomer detector location, the scaling providing the higher value. Thus a bias factor of about 0.934 should be applied to all the adjoint-scaled downcomer dosimeter end-of-cycle activity contributions from the last source distribution, and factors intermediate between 0.934 and unity probably exist for source distributions between Nos. 5 and 8. For time intervals prior to that of the reference source, however, the source distributions in the multiply burned peripheral assemblies would produce less leakage relative to their contribution in the reference distribution than would the source distributions in the peripheral assemblies containing fresh fuel since the leakage increases at a faster rate with cycle 9 exposure for the burned peripheral assemblies than for the fresh assemblies. Consequently, the bias factors correcting the adjoint-scaled fluxes at the 20-deg downcomer detector location lie above unity for end-of-cycle activity contributions from time intervals occurring before that of the reference source. As a result, the bias factors from this effect tend to cancel each other over the duration of the cycle. Since the activities are more sensitive to the source distributions near the end of the cycle than those near the beginning, the cancellation is not complete. The resulting net correction factor is estimated to be close enough to unity that it will be neglected, however.

II.E. Calculated End-of-Cycle Activities and Comparison with Measurements

Results of the end-of-cycle dosimeter activities as calculated by the TIMEPATCH module are compared with the measurements in Table V. Values from ENDF/B-V of 0.06 and 0.06267 were used for ^{137}Cs yields from fission in ^{238}U and ^{237}Np respectively. After the estimated contributions from several competing reactions in the measurements are considered, the calculated-to-measured ratios for the different reactions at a given

Table V. Comparison of Calculated and Measured End-of-Cycle Activities

Activity in dps/atom						
	$^{63}\text{Cu}(n,\alpha)^{60}\text{Co}$	$^{46}\text{Ti}(n,p)^{46}\text{Sc}$	$^{54}\text{Fe}(n,p)^{54}\text{Mn}$	$^{58}\text{Ni}(n,p)^{58}\text{Co}$	$^{238}\text{U}(n,f)^{137}\text{Cs}$	$^{237}\text{Np}(n,f)^{137}\text{Cs}$
<u>Downcomer Location</u>						
Calculated	3.26-18 ^a	2.78-16	1.23-15	2.21-15	1.60-17	1.19-16
Measured	3.94-18 ^b	3.44-16	1.49-15	2.55-15	2.00-17 ^c	1.40-16 ^d
C/E	0.83	0.81	0.83	0.87	0.80	0.85
<u>0-deg Cavity Location</u>						
Calculated	2.84-20	2.13-18	9.43-18	1.85-17	1.97-19	5.10-18
Measured	3.94-20 ^b	3.25-18	1.39-17	2.80-17	3.02-19 ^e	8.36-18 ^f
C/E	0.72	0.66	0.68	0.66	0.65	0.61

16

^aRead as 3.26×10^{-18} .

^bCorrected for an estimated 2.5% contribution from the $^{59}\text{Co}(n,\gamma)^{60}\text{Co}$ reaction.

^cCorrected for an estimated 5% contribution from photofission.

^dCorrected for an estimated 2.5% contribution from photofission.

^eCorrected for an estimated 10% contribution from photofission.

^fCorrected for an estimated 5% contribution from photofission.

location are seen to be quite consistent with one another. The average C/E values of 0.83 and 0.66 at the two locations indicate the presence of underpredictory elements in the calculation, however, which have also consistently occurred in past analyses of the PCA and PSF benchmark experiments² as well as the ANO-1 reactor,³ and which have been ascribed principally to inaccuracies in the ENDF/B-V total iron inelastic cross section (see Section III).

A comparison of calculated and measured axial cavity profiles at 0 deg is shown in Table VI. The measurements consisted primarily of counting the stainless steel dosimetry supporting wires, but these results were supplemented by analysis of a few dosimeter foils as well. The comparisons indicate reasonable agreement between the wire and foil measurements (the wire measurements had poorer counting statistics and a less reproducible counting geometry) and, perhaps more significantly, good agreement between the calculated and measured profiles. The latter conclusion rests on the observation that the off-midplane comparisons are no worse than the mid-plane values. Since no higher quadrature set was used in the R-Z transport calculation in the cavity than anywhere else (a symmetric S₈ set was used throughout), it can be concluded that there is no streaming problem in the HBR-2 cavity, provided the R-Z calculation uses a cavity geometry that includes the 0-deg detector well. An even stronger statement might conclude that the agreement with the measured relative axial distribution suggests that, at least over the range of heights investigated, streaming is not the basic mechanism for transporting neutrons up and down the cavity, but rather the axial distribution of the core source itself, and that the presence of the detector well does not significantly influence the axial distribution in the cavity.

This stronger premise can be investigated by comparing the measured and calculated axial profiles at 12 deg in the cavity. At this azimuth, the detector well no longer exists (see Fig. 1). The same R-Z calculations used to analyze the 0-deg detector, which contain in their geometric description an artificially wide cavity since they include in addition an azimuthally independent detector well, can also be used to analyze the 12-deg detector location. From the resulting comparisons, presented in Table VII, it appears that, with possible exceptions near the very top of the profile, the calculated and measured profiles again are in good agreement, hence tending to verify the conclusion that the presence of the detector well does not significantly affect the axial distribution. It still contributes a significant effect in the R- θ calculation, however, where the absence of a strong reflecting surface at 0 and 45 deg reduces the back-scattered component at these cavity locations.

II.F. Calculated End-of-Cycle Critical Pressure Vessel Fluences

The group fluences accumulated over cycle 9 at each of two critical pressure vessel locations are shown in Table VIII in the ELXSIR group structure for all energies lying above 0.1 MeV.

Table VI. Comparison of Calculated and Measured Axial Profiles of End-of-Cycle Activities at 0 deg in the Cavity

Distance Above Midplane (cm)	dps/iron target atom			C/E	dps/nickel target atom			C/E
	WIRE	FOIL	CALC		WIRE	FOIL	CALC	
213		1.53-18 ^a						
190 ^b	3.49-18		2.50-18	0.72	8.19-18		4.93-18	0.60
160	8.38-18		5.1 -18	0.61	1.70-17		1.02-17	0.60
130 ^c	1.19-17		7.4 -18	0.62	2.37-17		1.45-17	0.61
107		1.24-17	8.43-18	0.68				
84	1.51-17		8.8 -18	0.58	3.10-17		1.75-17	0.56
53	1.29-17		9.1 -18	0.70	2.85-17		1.80-17	0.63
23	1.47-17		9.3 -18	0.63	2.95-17		1.85-17	0.63
0		1.39-17	9.43-18	0.68		2.80-17	1.85-17	0.66
-23	1.41-17		9.5 -18	0.67	2.96-17		1.85-17	0.63
-53	1.44-17		9.4 -18	0.65	2.85-17		1.85-17	0.65
-84	1.51-17		9.4 -18	0.62	2.82-17		1.82-17	0.65
-107		1.43-17	9.07-18	0.63				
-130 ^c	1.24-17		8.3 -18	0.67	2.69-17		1.63-17	0.61
-160	8.85-18		5.9 -18	0.67	1.96-17		1.19-17	0.61
-190 ^b	4.05-18		2.78-18	0.69	8.04-18		5.46-18	0.68
-213		1.09-18						

^aRead as 1.53×10^{-18} .

^bApproximate limits of the active core.

^cApproximate limits defining the flat axial profile region of the source.

Table VII. Comparison of Calculated and Measured Axial Profiles of End-of-Cycle Activities at 12 deg in the Cavity

Distance Above Midplane (cm)	dps/iron target atom			C/E	dps/nickel target atom		C/E
	WIRE	FOIL	CALC		WIRE	CALC	
206	1.35-18 ^a		1.29-18	0.96	2.69-18	2.56-18	0.95
175 ^b	3.76-18		3.31-18	0.88	8.87-18	6.53-18	0.74
145 ^c	7.46-18		5.74-18	0.77	1.52-17	1.12-17	0.74
84	9.29-18		7.75-18	0.83	2.01-17	1.51-17	0.75
53	1.20-17		8.06-18	0.67	2.29-17	1.57-17	0.69
23	1.12-17		8.20-18	0.73	2.38-17	1.60-17	0.67
0		1.07-17	8.26-18	0.77			
-23	1.32-17		8.3 -18	0.63	1.87-17	1.63-17	0.87
-53	1.09-17		8.3 -18	0.76	2.65-17	1.63-17	0.62
-84	1.25-17		8.2 -18	0.66	2.33-17	1.59-17	0.68
-114	1.28-17		7.8 -18	0.61	2.09-17	1.50-17	0.72
-145 ^c	8.98-18		6.2 -18	0.69	1.81-17	1.2 -17	0.66
-175 ^b	5.19-18		3.83-18	0.74	1.12-17	7.48-18	0.67
-206	1.89-18				4.16-18		

^aRead as 1.35×10^{-18} .

^bApproximate limits of the active core.

^cApproximate limits defining the flat axial profile region of the source.

Table VIII. Fluences Accumulated During Cycle 9 for Two Critical Pressure Vessel Locations

Group	Lower Energy (MeV)	Fluence in $n \cdot \text{cm}^{-2}$		Group	Lower Energy (MeV)	Fluence in $n \cdot \text{cm}^{-2}$	
		LCW	T/4			LCW	T/4
1	14.2	1.19+14 ^a	4.66+13	20	2.12	2.41+16	1.19+16
2	12.2	5.90+14	2.37+14	21	1.92	4.53+16	2.25+16
3	11.1	7.60+14	3.01+14	22	1.83	2.30+16	1.29+16
4	10.0	1.71+15	6.70+14	23	1.65	5.43+16	3.13+16
5	8.61	5.05+15	1.95+15	24	1.50	5.13+16	2.96+16
6	8.19	2.36+15	9.06+14	25	1.35	5.70+16	3.62+16
7	7.41	6.56+15	2.44+15	26	1.23	5.36+16	3.50+16
8	7.05	3.68+15	1.38+15	27	1.00	1.16+17	8.88+16
9	6.07	1.78+16	6.35+15	28	0.907	5.43+16	4.73+16
10	4.97	3.03+16	1.04+16	29	0.821	5.93+16	4.79+16
11	4.07	3.77+16	1.29+16	30	0.743	6.06+16	4.30+16
12	3.68	1.79+16	6.39+15	31	0.608	1.74+17	1.91+17
13	3.01	4.43+16	1.67+16	32	0.498	1.37+17	1.33+17
14	2.73	3.48+16	1.42+16	33	0.369	1.72+17	1.94+17
15	2.59	2.03+16	8.85+15	34	0.302	1.47+17	1.81+17
16	2.47	2.04+16	8.45+15	35	0.213	1.71+17	1.76+17
17	2.37	2.08+16	8.93+15	36	0.183	6.13+16	5.96+16
18	2.35	5.94+15	2.76+15	37	0.111	1.93+17	1.92+17
19	2.23	2.77+16	1.35+16	38	0.098	3.45+16	3.04+16

^aRead as 1.19×10^{14} .

III. ESTIMATED UNCERTAINTIES IN THE CALCULATED RESULTS

The LEPRICON procedure identifies and treats various sources of uncertainty that from previous experience in the development of the benchmark data base,² as well as from the analysis of the ANO-1 reactor,³ can lead to non-negligible uncertainties in the calculated pressure vessel fluxes and dosimeter activities. For the particular application to HBR-2, six bias factors in addition to three types of nuclear data were considered in contributing to the covariances of the calculated quantities that were presented in Section II.

The nuclear data considered, standard for all applications, are the total inelastic cross sections of the major components of steel, the spectrum arising from thermal fission of ^{235}U , and the reaction cross sections of the various dosimeters. Since iron is a major component of all steels, and the uncertainties in the chromium and nickel total inelastic cross sections are comparable with those in the iron cross section, in the LEPRICON system we have introduced the concept of the uncertainty in the total steel inelastic cross section in which the contributions from the chromium and nickel in stainless steel are treated as having arisen from additional amounts of iron. Thus the simplification assumes the form of using uncertainties in the iron data only and folding them with flux sensitivities derived by approximating all steels (i.e., derivatives of both carbon steel and stainless steel) as being composed of pure iron. This procedure tends to underpredict the resulting flux uncertainties from those obtained by summing the individual components because of the somewhat larger uncertainties of chromium and nickel, but not significantly so.

The flux sensitivities to the total iron inelastic cross section used as part of the data base are the result of parameterizing results previously obtained for the benchmark and ANO-1 analyses in terms of a total iron thickness penetrated between source and detector location.¹¹ The parameterized sensitivities agree with the calculated values to within about 10 percent for those elements of the sensitivity matrix which lead to significant contributions to the flux covariances.

Effects produced by uncertainties in the spectrum arising from ^{235}U thermal fission are significant only for the higher energy fluxes ($E > 6\text{MeV}$) and then only when there is little iron between the core and the detector. Although a fission spectrum intermediate between that of ^{235}U and ^{239}Pu was used in the transport calculation to better describe the neutron source energy distribution in the highly important twice-burned peripheral fuel assemblies at 0-deg azimuth, there is at most only a 15 percent difference between the two isotopic spectra and hence little change in the uncertainties of the spectrum used compared with those of ^{235}U alone.

Flux sensitivities to the fission spectrum appearing in LEPRICON are again the result of a parameterization effort which led to the adoption of a "universal" sensitivity profile that is the same for all detector locations and penetration geometry.¹¹ Again the parameterized sensitivities agree with the calculated values to within about 10 percent for the more important matrix elements.

Uncertainties in the dosimeter reaction cross sections, with one exception, constitute the least important of the types of nuclear data retained in the analysis. Only the $^{237}\text{Np}(n,f)$ cross section has an appreciable uncertainty associated with it, a probably overly conservative standard deviation of around 10 percent; the remaining reaction cross section covariances are insignificant in contributing to the uncertainties of the calculated dosimeter activities when compared with covariances derived for the flux.

The six bias factors deemed applicable to the HBR-2 analysis are listed in Table IX along with their assumed flux correlations. The uncertainties in the geometric and materials data which give rise to the flux uncertainties are based on discussions with qualified researchers¹² as well as our own limited experience, and their propagated contributions to the flux uncertainties were obtained from one-dimensional transport calculations. It should be emphasized that these multiplicative bias factors all have a priori values of unity for the group fluxes, but because of their uncertainties the a posteriori values are in general different from unity. Because of the insignificant contribution from uncertainties in the source distributions observed in the ANO-1 analysis and the excellent agreement between measured and calculated assembly powers routinely achieved by CP&L,¹³ the effects of source uncertainties on the fluxes at various locations in HBR-2 were not calculated and assumed to be negligible.

The contributions to the flux uncertainties from each of the applicable types of nuclear data and geometric and materials data to the downcomer dosimeter location listed in Table IX are summarized in Table X in the standard LEPRICON adjustment module group structure.¹¹ It can be seen that the contributions from uncertainties in the fission spectrum at high energies, in the total inelastic cross sections of the major steel components, and in the absolute location of the dosimetry dominate the estimated flux uncertainties which at 22 percent are virtually independent of energy.

A similar breakdown of the various contributions to the flux uncertainties at the 0-deg midplane cavity dosimetry location is shown in Table XI. Here the uncertainties in the steel total inelastic cross section dominate those from all other sources, accounting for virtually all of the flux uncertainties above 0.9 MeV. Only the contribution from the pressure vessel out-of-roundness bias factor at energies below 0.9 MeV prevents the complete domination of the inelastic cross section contribution at all energies above 0.1 MeV. Flux uncertainties in the cavity are seen to lie in the range of 20 to 35 percent, with the larger values occurring at the higher energies.

The contributions from the various assumed sources of uncertainty at both the critical LCW and T/4 locations in the pressure vessel appear in Table XII. The estimated group flux total uncertainties at both locations are seen to be closely the same, with a limited dependence on energy from about 16 to 22 percent. At either location, significant contributions from the fission spectrum are limited to the first two groups, while the combined effects from uncertainties in the total inelastic cross section and pressure vessel out-of-roundness account for most of the flux uncertainties throughout the complete energy range of interest.

Table IX. Flux Bias Factors Assumed in the Calculations and Their Correlations

Bias Factor	Source of Bias Factor Uncertainty	Locations	Complete Flux Correlations	
			Auto	Cross
1	Dosimetry capsule location	Downcomer only	0.9	
2	Finite capsule perturbation	Downcomer only	0.9	
3	Pressure vessel out-of-roundness	Cavity and pressure vessel	0.9	0.81 ^a
4	Coolant density	Downcomer, cavity and pressure vessel	0.9	0.81 ^b
5	Three-dimensional flux synthesis	Downcomer, cavity and pressure vessel	0.75	0.375-0.675 ^c
6	Steel density	Downcomer, cavity and pressure vessel	0.9	0.18-0.54 ^d

^aFor combinations involving either pressure vessel location.

^bFor combinations involving either pressure vessel location with either dosimetry location, as well as between the two dosimetry locations.

^c0.375 between downcomer and LCW locations and between LCW and cavity locations;
0.525 between downcomer and cavity locations and between downcomer and T/4 locations;
0.675 between T/4 and cavity locations.

^d0.18 between downcomer and cavity locations; 0.27 between either pressure vessel location and cavity location; 0.54 between downcomer location and either pressure vessel location.

Table X. Standard Deviations in the Fluxes at the Downcomer Dosimeter Location Arising from Parameter Uncertainties

Flux Group	Lower Energy (MeV)	Standard Deviation (%)							
		χ_{25}	$\sigma_{\text{steel}}(n, n')$	BF1	BF2	BF4	BF5	BF6	Total
1	11.1	14.1	13.2	10.9	1.0	3.1	1.5	3.0	22.7
2	8.2	10.6	13.7	12.1	1.0	3.4	1.5	3.1	21.7
3	6.1	8.1	13.3	13.3	1.0	3.8	1.5	3.4	21.2
4	4.1	6.4	14.3	14.7	1.0	4.2	1.5	3.6	22.3
5	3.0	6.1	13.2	17.0	2.0	5.0	1.5	3.5	23.3
6	2.6	5.5	9.7	17.8	2.5	5.3	1.5	3.3	22.1
7	2.1	5.1	9.5	18.0	3.0	5.7	1.5	3.2	22.2
8	1.8	5.2	9.2	18.3	3.5	6.0	1.5	3.1	22.5
9	1.5	5.2	8.8	19.3	3.5	6.3	1.5	3.0	23.3
10	1.2	5.1	8.9	19.5	4.0	6.5	1.5	2.9	23.5
11	0.9	5.2	8.0	20.3	4.5	6.9	1.5	2.6	24.1
12	0.6	5.1	5.4	20.5	5.0	7.2	1.5	2.4	23.7
13	0.4	5.1	5.4	20.2	5.5	7.6	1.5	2.1	23.6
14	0.2	5.1	5.4	19.8	6.0	7.7	1.5	1.9	23.4
15	0.1	5.1	5.3	18.4	6.5	7.5	1.5	1.9	22.3

Table XI. Standard Deviations in the Fluxes at the Cavity Dosimeter Location Arising from Parameter Uncertainties

Flux Group	Lower Energy (MeV)	Standard Deviation (%)						
		X25	$\sigma_{\text{steel}(n,n^{\prime})}$	BF3	BF4	BF5	BF6	Total
1	11.1	14.1	29.6	6.7	3.7	2.5	5.5	34.3
2	8.2	10.6	30.8	7.3	4.0	2.5	5.8	34.3
3	6.1	8.1	29.8	7.9	4.4	2.5	6.3	32.9
4	4.1	6.4	32.2	8.6	4.9	2.5	6.6	35.0
5	3.0	6.1	29.8	9.2	5.5	2.5	6.4	33.0
6	2.6	5.5	21.8	9.6	5.7	2.5	6.2	26.0
7	2.1	5.1	21.3	9.9	6.0	2.5	6.0	25.6
8	1.8	5.2	20.6	9.9	6.0	2.5	5.8	25.0
9	1.5	5.2	19.9	10.1	6.2	2.5	5.5	24.5
10	1.2	5.1	20.0	10.2	6.3	2.5	5.2	24.6
11	0.9	5.2	18.0	10.3	6.5	2.5	4.5	22.9
12	0.6	5.1	12.0	10.5	6.4	2.5	3.8	18.5
13	0.4	5.1	12.0	10.6	6.9	2.5	3.4	18.7
14	0.2	5.1	12.2	10.7	6.9	2.5	2.8	18.7
15	0.1	5.1	12.0	10.7	7.1	2.5	2.8	18.7

Table XII. Standard Deviations in the Fluxes at the Critical
LCW and T/4 Pressure Vessel Locations Arising
from Parameter Uncertainties

Flux Group	Lower Energy (MeV)	Standard Deviation (%)									
		x25	$\sigma_{\text{steel}}(n,n')$		BF3	BF4	BF5		BF6	Total	
			LCW	T/4			LCW	T/4		LCW	T/4
1	11.1	14.1	11.4	15.9	6.8	3.7	5.0	1.5	3.0	20.6	22.9
2	8.2	10.6	11.9	16.5	7.4	4.1	5.0	1.5	3.1	19.0	21.7
3	6.1	8.1	11.5	16.0	7.9	4.5	5.0	1.5	3.4	17.8	20.4
4	4.1	6.4	12.4	17.3	8.6	5.0	5.0	1.5	3.6	18.2	21.3
5	3.0	6.1	11.4	15.9	9.5	5.7	5.0	1.5	3.5	18.1	20.7
6	2.6	5.5	8.4	11.7	10.0	6.0	5.0	1.5	3.3	16.5	17.8
7	2.1	5.1	8.2	11.4	10.2	6.3	5.0	1.5	3.2	16.5	17.7
8	1.8	5.2	8.0	11.0	10.3	6.3	5.0	1.5	3.1	16.5	17.5
9	1.5	5.2	7.7	10.7	10.5	6.5	5.0	1.5	3.0	16.5	17.4
10	1.2	5.1	7.7	10.7	10.6	6.5	5.0	1.5	2.9	16.5	17.5
11	0.9	5.2	6.9	9.6	10.6	6.6	5.0	1.5	2.6	16.2	16.9
12	0.6	5.1	4.7	6.5	10.9	6.5	5.0	1.5	2.4	15.5	15.4
13	0.4	5.1	4.7	6.5	10.9	7.0	5.0	1.5	2.1	15.7	15.6
14	0.2	5.1	4.7	6.6	10.9	7.0	5.0	1.5	1.9	15.6	15.6
15	0.1	5.1	4.6	6.4	10.9	7.2	5.0	1.5	1.9	15.7	15.6

The autocorrelation matrices of the calculated group fluxes at the two dosimeter and two pressure vessel locations are shown in Tables XIII-XVI. It is to be observed that the fluxes at any one location are rather highly correlated, and that the pattern of these correlations is similar for all four locations. With the exception of the first two groups which exhibit a somewhat anomalous behavior because of the importance of the fission spectrum uncertainty in this region, the individual spectra are about 80 percent or more correlated. These observations are generally in agreement with those deduced from the analysis of ANO-1, but with some differences in the degree of correlation of the cavity spectra.

The complete correlation matrix of the calculated activities is shown in Table XVII, where high degrees of correlation are seen to exist both among the activities at a given dosimetry location (the autocorrelations) and between the activities at different locations (the cross correlations). This is primarily due, of course, to the significant uncertainties in the steel total inelastic cross section that are propagated to all energies via the transport process and hence represent a strong source of correlation among all the calculated fluxes. The standard deviations of the calculated activities are seen from Table XVII to vary from about 20 percent at the downcomer location to about 30 percent in the cavity.

As a final illustration of the results of the LEPRICON procedure for estimating the á priori covariances for HBR-2, the cross correlation matrix between both sets of critical pressure vessel fluxes and both sets of dosimeter activities is presented in Table XVIII. As was first pointed out in Ref. 3, the elements of this matrix determine the effectiveness of the adjustment procedure, for they indicate the degree to which the pressure vessel fluxes are influenced by changes in the calculated activities when comparisons of calculated and measured activities at in-vessel or ex-vessel locations are made. Reasonably high values for these cross correlations are sine qua non to the success of the entire LEPRICON methodology. The entries in Table XVIII vary between 0.3 and 0.8 which, while not overwhelming, are probably adequate. It should be noted that the critical T/4 fluxes enjoy a slightly higher correlation with the activities at either dosimeter location than the LCW fluxes do, and, far more significantly, the cavity dosimeter location is clearly superior in providing information concerning flux levels in the pressure vessel. To some extent, this conclusion may be the result of ascribing a perhaps too large uncertainty to the absolute radial location of the downcomer surveillance capsule (estimated to be 12.7 mm or 0.5 in.¹²), but the general advantages of cavity dosimetry over downcomer dosimetry still remain apparent because the cavity activities possess the higher sensitivities to the same sources of uncertainty that influence the fluxes in the pressure vessel, such as the steel inelastic cross section and the pressure vessel out-of-roundness bias factor, and at the same time no sensitivity to the location of the downcomer capsule which the pressure vessel fluxes are also insensitive to.

Table XIII. Autocorrelation Matrix of the Calculated Group Fluxes at the Downcomer Dosimetry Location*

Flux Group	Lower Energy (MeV)	SD (%)	1	2	3	4	5	6	7	8	9	10	11	12	13	14	15
1	11.1	22.7	100 ^a														
2	8.2	21.7	94	100													
3	6.1	21.2	66	67	100												
4	4.1	22.3	57	58	94	100											
5	3.0	23.3	58	60	93	94	100										
6	2.6	22.1	62	65	85	85	88	100									
7	2.1	22.2	61	64	81	82	85	92	100								
8	1.8	22.5	62	65	82	82	86	92	52	100							
9	1.5	23.3	61	65	81	82	85	92	92	92	100						
10	1.2	23.5	62	65	81	82	85	91	92	92	92	100					
11	0.9	24.1	62	65	81	82	86	90	90	91	91	91	100				
12	0.6	23.7	59	63	79	80	84	87	86	87	88	88	90	100			
13	0.4	23.6	59	63	79	80	84	87	86	87	88	88	89	91	100		
14	0.2	23.4	59	62	78	79	84	86	86	87	87	88	89	91	91	100	
15	0.1	22.3	59	62	78	79	84	86	85	87	87	88	89	91	91	91	100

*Matrix is symmetric; only the lower half is shown.
^aAll elements have been multiplied by 100.

Table XIV. Autocorrelation Matrix of the Calculated Group Fluxes at the Cavity Dosimetry Location*

Flux Group	Lower Energy (MeV)	SD (%)	1	2	3	4	5	6	7	8	9	10	11	12	13	14	15
1	11.1	34.3	100 ^a														
2	8.2	34.3	96	100													
3	6.1	32.9	42	40	100												
4	4.1	35.0	29	27	98	100											
5	3.0	33.3	31	29	97	98	100										
6	2.6	26.0	39	37	84	83	85	100									
7	2.1	25.6	40	37	75	74	76	96	100								
8	1.8	25.0	40	38	78	77	79	97	97	100							
9	1.5	24.5	41	39	78	77	79	96	97	97	100						
10	1.2	24.6	42	40	79	78	80	96	96	97	97	100					
11	0.9	22.9	45	42	84	83	85	94	92	93	94	95	100				
12	0.6	18.5	38	36	86	86	87	82	76	79	80	81	87	100			
13	0.4	18.6	38	36	85	85	87	82	76	79	80	81	86	95	100		
14	0.2	18.7	37	35	85	85	87	82	76	79	80	80	86	95	95	100	
15	0.1	18.7	37	35	85	85	87	81	76	78	80	80	86	94	95	95	100

*Matrix is symmetric; only the lower half is shown.

^aAll elements have been multiplied by 100.

Table XV. Autocorrelation Matrix of the Calculated Group Fluxes at the Critical LCW Pressure Vessel Location*

Flux Group	Lower Energy (MeV)	SD (%)	1	2	3	4	5	6	7	8	9	10	11	12	13	14	15
1	11.1	20.6	100 ^a														
2	8.2	19.0	94	100													
3	6.1	17.8	67	66	100												
4	4.1	18.2	56	56	94	100											
5	3.0	18.1	57	58	93	94	100										
6	2.6	16.5	61	63	85	85	87	100									
7	2.1	16.5	61	62	80	80	83	92	100								
8	1.8	16.5	61	63	81	81	84	92	92	100							
9	1.5	16.5	61	63	81	81	84	92	92	92	100						
10	1.2	16.5	62	64	81	81	84	92	92	92	92	100					
11	0.9	16.2	63	65	83	83	86	91	90	90	91	91	100				
12	0.6	15.5	61	63	81	82	84	86	85	86	86	86	88	100			
13	0.4	15.7	61	63	81	81	84	86	84	85	86	86	88	90	100		
14	0.2	15.6	60	62	81	81	84	86	84	85	86	86	88	90	90	100	
15	0.1	15.7	60	62	80	81	84	85	84	85	86	86	88	90	90	90	100

*Matrix is symmetric; only the lower half is shown.

^aAll elements have been multiplied by 100.

Table XVI. Autocorrelation Matrix of the Calculated Group Fluxes at the Critical T/4 Pressure Vessel Location*

Flux Group	Lower Energy (MeV)	SD (%)	1	2	3	4	5	6	7	8	9	10	11	12	13	14	15
1	11.1	22.9	100 ^a														
2	8.2	21.7	96	100													
3	6.1	20.4	56	55	100												
4	4.1	21.3	44	42	96	100											
5	3.0	20.7	46	45	96	97	100										
6	2.6	17.8	53	52	85	84	87	100									
7	2.1	17.7	52	52	78	78	80	94	100								
8	1.8	17.5	53	53	80	79	82	95	95	100							
9	1.5	17.4	54	53	80	79	82	94	94	95	100						
10	1.2	17.5	54	54	80	80	83	94	94	94	94	100					
11	0.9	16.9	56	56	83	83	86	93	91	92	93	93	100				
12	0.6	15.4	53	53	81	81	85	85	82	84	85	85	89	100			
13	0.4	15.6	52	52	81	81	84	85	82	84	85	85	88	93	100		
14	0.2	15.6	52	52	81	81	84	85	82	84	85	85	88	93	93	100	
15	0.1	15.6	52	52	81	81	84	85	82	84	85	85	88	93	93	93	100

*Matrix is symmetric; only the lower half is given.
^aAll elements have been multiplied by 100.

Table XVII. Complete Correlation Matrix of the Calculated Activities*

	SD (%)	Downcomer Location						Cavity Location					
		⁶³ Cu	⁴⁶ Ti	⁵⁴ Fe	⁵⁸ Ni	²³⁸ U	²³⁷ Np	⁶³ Cu	⁴⁶ Ti	⁵⁴ Fe	⁵⁸ Ni	²³⁸ U	²³⁷ Np
Downcomer Location													
⁶³ Cu	19.7	100 ^a											
⁴⁶ Ti	20.3	96	100										
⁵⁴ Fe	20.9	93	98	100									
⁵⁸ Ni	21.0	93	97	99	100								
²³⁸ U	21.2	89	92	96	97	100							
²³⁷ Np	23.9	79	82	86	87	90	100						
Cavity Location													
⁶³ Cu	30.6	87	82	76	75	69	59	100					
⁴⁶ Ti	31.7	84	87	83	82	74	62	95	100				
⁵⁴ Fe	32.0	80	86	87	86	80	68	87	96	100			
⁵⁸ Ni	31.4	80	86	88	87	82	69	86	95	100	100		
²³⁸ U	30.0	78	82	86	86	86	74	80	88	95	96	100	
²³⁷ Np	29.0	76	80	83	83	83	89	73	80	85	87	89	100

*Matrix is symmetric; only the lower half is given.

^aAll elements have been multiplied by 100.

Table XVIII. Cross-Correlation Matrix Between the Calculated Critical Pressure Vessel Fluxes and the Dosimeter Activities

Flux Group	Lower Energy (MeV)	Downcomer Location						Cavity Location					
		⁶³ Cu	⁴⁶ Ti	⁵⁴ Fe	⁵⁸ Ni	²³⁸ U	²³⁷ Np	⁶³ Cu	⁴⁶ Ti	⁵⁴ Fe	⁵⁸ Ni	²³⁸ U	²³⁷ Np
1	11.1	58 ^a (59) ^b	46(46)	36(35)	35(34)	31(31)	25(24)	67(72)	53(56)	40(41)	40(40)	37(37)	33(31)
2	8.2	56(56)	44(43)	33(32)	33(32)	29(28)	23(22)	69(74)	54(57)	40(40)	40(40)	38(37)	33(31)
3	6.1	59(62)	61(66)	57(62)	56(60)	47(49)	36(38)	69(74)	76(82)	75(82)	73(80)	65(69)	57(60)
4	4.1	53(55)	58(62)	56(60)	55(59)	45(48)	35(36)	64(67)	74(79)	76(82)	74(80)	65(69)	58(60)
5	3.0	51(54)	56(60)	54(59)	53(57)	44(47)	34(36)	62(66)	71(77)	73(80)	72(78)	64(69)	58(60)
6	2.6	44(48)	46(51)	45(51)	45(50)	42(47)	32(36)	55(60)	59(66)	63(71)	64(72)	64(72)	54(58)
7	2.1	41(44)	42(46)	42(46)	41(46)	40(45)	31(34)	51(56)	54(61)	59(66)	60(67)	63(70)	52(56)
8	1.8	42(45)	43(47)	42(48)	42(47)	41(45)	32(35)	52(57)	55(62)	59(67)	60(68)	63(70)	53(57)
9	1.5	42(45)	42(47)	42(47)	42(47)	40(45)	32(35)	52(57)	55(62)	58(66)	60(67)	62(70)	53(57)
10	1.2	42(46)	43(48)	42(48)	42(47)	40(45)	32(35)	52(58)	55(62)	59(67)	60(68)	62(70)	53(57)
11	0.9	43(48)	44(50)	43(49)	43(48)	40(45)	32(35)	53(60)	57(65)	59(68)	60(68)	60(68)	54(58)
12	0.6	39(44)	40(47)	39(45)	38(44)	34(39)	28(32)	47(54)	51(59)	52(61)	52(61)	51(57)	51(56)
13	0.4	39(44)	40(46)	39(45)	38(44)	34(39)	28(32)	47(53)	51(59)	52(61)	52(60)	51(57)	50(55)
14	0.2	39(44)	41(47)	39(45)	38(44)	34(39)	28(32)	47(54)	51(59)	52(61)	53(61)	51(58)	50(55)
15	0.1	39(43)	40(46)	38(44)	38(43)	34(38)	28(31)	47(53)	51(59)	52(61)	52(60)	51(57)	50(55)

^aAll elements have been multiplied by 100.

^bThe LCW flux cross correlations appear first, followed by the T/4 flux cross correlations in parentheses.

IV. ESTIMATED UNCERTAINTIES IN THE MEASUREMENTS

Following the procedure outlined in Ref. 3, covariances of the 12 dosimeter measurements in HBR-2 were estimated with the help of the experimentalists.¹⁴ Four sources of uncertainty were identified: random counting statistics, gamma-ray counter efficiency calibrations, bias factors arising from estimated contributions to the measured activities from competing reactions, and normalization of the measured activities during exposure to one core neutron per second, as required by the LEPRICON adjustment module. Each of these sources is analyzed in the following subsections.

IV.A. Random Counting Uncertainties

As was the case in ANO-1, statistical variations in the measured counting rates may be assumed to be virtually negligible except for the case of the low $^{63}\text{Cu}(n,\alpha)^{60}\text{Co}$ and $^{238}\text{U}(n,f)^{137}\text{Cs}$ activities, for which standard deviations of 1 percent may be assumed.

IV.B. Systematic Efficiency Uncertainties

Standard deviations estimated at 4 percent^b arise from uncertainties in the efficiency calibration and energy interpolation of the gamma-ray counter. As in Ref. 3, the correlations between gamma rays (and hence reactions) are assumed to be a function of the proximity of the two gamma-ray energies. For the same reaction, correlation coefficients of 0.7 (and not unity) are assumed between the two dosimeter locations in the reactor because of the use of different shelf calibrations in the counter. For different reactions, the efficiency correlations are presented in Table XIX along with a list of the gamma rays that were counted. All correlations not specifically appearing in this table are assumed to be negligible. Finally, cross correlations between different reactions at different dosimeter locations in the reactor are assumed to be one-half the product of the correlation between the reactions at the same location and the correlation between the same reactions at the two locations. Thus, as for a similar situation among different experiments that arose in ANO-1, it is being assumed that one-half of the covariance between two different reactions at the same reactor location and one-half of the covariance between the same reaction at different reactor locations arise from a common source of uncertainty. Under the assumptions given, these cross correlations become equal to 0.35 of the values appearing in Table XIX and are symmetric (i.e., the cross correlation between reaction A at location 1 and reaction B at location 2 is the same as that between reaction B at location 1 and reaction A at location 2).

^bThis represents a somewhat more conservative value than the value of about 2.5 percent estimated by Ref. 14.

Table XIX. Gamma Rays Counted for Each Reaction and Assumed Efficiency Energy Correlations

Reaction	Gamma Rays Counted (keV)	Energy Correlation
$^{63}\text{Cu}(n,\alpha)^{60}\text{Co}$	1173 and 1332	1.0 (Average Taken)
$^{46}\text{Ti}(n,p)^{46}\text{Sc}$	889	0.7 with ^{54}Mn
$^{54}\text{Fe}(n,p)^{54}\text{Mn}$	835	0.9 with ^{58}Co
$^{58}\text{Ni}(n,p)^{58}\text{Co}$	811	0.5 with ^{46}Sc
$^{238}\text{U}(n,f)^{137}\text{Cs}$	662	} 1.0
$^{237}\text{Np}(n,f)^{137}\text{Cs}$	662	

IV.C. Bias Factor Uncertainties

Several reaction-dependent bias factors were applied subsequent to the final reduced end-of-cycle activities provided by Ref. 14. Unlike the bias factors introduced into the calculations, the measurement bias factors are generally different from unity and represent estimated corrections to the measured values that account for the contribution from other competing reactions leading to the same unstable reaction product. The first example involves an estimated 2.5 percent correction to the $^{63}\text{Cu}(n,\alpha)^{60}\text{Co}$ measurements arising from a possible contribution from the $^{59}\text{Co}(n,\gamma)^{60}\text{Co}$ reaction, based on an analysis performed for the ANO-1 reactor that indicated at most a 5 percent effect.³ Thus a bias factor of 0.975 with an uncertainty of 2.5 percent is assumed for HBR-2 as well, with no correlation at the two reactor locations since the thermal flux to fast flux ratios are obviously different.

A second example involves possible contributions from photofission reactions in both the $^{238}\text{U}(n,f)$ and $^{237}\text{Np}(n,f)$ measurements. Based on previous gamma-ray analysis of benchmark experiments performed in geometries similar to those of PWRs¹⁵ and using the most recent values of photofission cross sections,¹⁶ estimated contributions from photofission may be obtained. This resulted in bias factors of 0.95 and 0.90 being applied at the downcomer and cavity locations respectively to correct the measured ^{137}Cs activities from ^{238}U . The corresponding uncertainties were 5 and 10 percent. No correlation between the two ^{238}U foil measurements was assumed because of the poorly known magnitude of the gamma-ray flux in the cavity relative to that in the downcomer. Similarly, less conservative bias factors of 0.975 and 0.95 were used at the downcomer and cavity locations respectively to correct the measured ^{137}Cs activities from ^{237}Np , with corresponding uncertainties of 2.5 and 5 percent, again with no correlation assumed between the two ^{237}Np foil measurements. However, a perfect correlation was assumed between the ^{238}U and ^{237}Np dosimeters at the same locations.

A second type of bias factor, this time assumed to be unity, also affects the uncertainty of the measurements. It arises as a result of neglect of possible coincidence summing corrections in both the calibration and foil counting stages as well as positioning uncertainties in the counter. These are assumed to contribute an additional uncorrelated 3 percent to the uncertainty of all the measurements.

IV.D. Normalization Uncertainties

The uncertainty in the absolute number of neutrons per second in the core averaged over the cycle 9 exposure is assumed to be composed of a 3 percent contribution arising from uncertainty in the conversion factor relating neutron production rate and reactor thermal power and a 2 percent contribution due to uncertainty in the reactor thermal power as determined from calibration of the in-core instrumentation. Since these two components are uncorrelated, the resulting uncertainty is 3.6 percent, which

is of course completely correlated among all the measurements. This uncertainty has traditionally been assigned to the measurements by the LEPRICON procedure, but conceptually it could just as logically be assigned to the calculations. The results of the adjustment procedure should be quite insensitive to the placement of this small uncertainty, however.

The resulting correlation matrix of the 12 dosimeter measurements from all sources of uncertainty is shown in Table XX. Although the cross correlations among the efficiencies are symmetric, it is to be noted that the overall cross correlations are not. As in the case of ANO-1, the standard deviations of the calculated activities (see Table XVII) are from three to five times greater than those of the measurements, and the corresponding correlations are also larger. Both of these factors result in appreciably larger covariances for the calculated quantities. It is for this reason that the measurements with their smaller uncertainties are so critically important in directing the course of the adjustment procedure to be described next.

Table XX. Complete Correlation Matrix of the Measured Activities*

	SD (%)	Downcomer Location						Cavity Location					
		⁶³ Cu	⁴⁶ Ti	⁵⁴ Fe	⁵⁸ Ni	²³⁸ U	²³⁷ Np	⁶³ Cu	⁴⁶ Ti	⁵⁴ Fe	⁵⁸ Ni	²³⁸ U	²³⁷ Np
Downcomer Location													
⁶³ Cu	6.72	100 ^a											
⁴⁶ Ti	6.16	31	100										
⁵⁴ Fe	6.16	31	64	100									
⁵⁸ Ni	6.16	31	55	72	100								
²³⁸ U	8.00	24	26	26	26	100							
²³⁷ Np	6.65	29	32	32	32	78	100						
Cavity Location													
⁶³ Cu	6.72	54	31	31	31	24	29	100					
⁴⁶ Ti	6.16	31	64	44	42	26	32	31	100				
⁵⁴ Fe	6.16	31	44	64	47	26	32	31	64	100			
⁵⁸ Ni	6.16	31	42	47	64	26	32	31	55	72	100		
²³⁸ U	11.79	16	18	18	18	26	24	16	18	18	18	100	
²³⁷ Np	7.93	24	27	27	27	29	46	24	27	27	27	84	100

*Matrix is symmetric; only the lower half is given.

^aAll elements have been multiplied by 100.

V. RESULTS OF THE ADJUSTMENT

In this section, the adjustments in the activities and the pressure vessel fluxes are presented for the optimum case of combining 11 of the 12 HBR-2 measurements simultaneously with the 34 measurements that constitute the benchmark data base. Combining all 12 measurements leads to a value of chi-square per degree of freedom for all 46 measurements of 1.15, which, although acceptable, is inferior to that previously obtained from other adjustments based on only the benchmark measurements² or the ANO-1 measurements in conjunction with the benchmark data.³ By "deactivating" (i.e., preventing from active participation in the adjustment procedure) the $^{237}\text{Np}(n,f)$ measurement in the HBR-2 cavity, one finds the resulting chi-square per degree of freedom for the 45 remaining measurements to be 1.00, a dramatic and significant reduction. The reason for the inconsistency of the $^{237}\text{Np}(n,f)$ cavity measurement is not difficult to discover, since the low calculated-to-measured ratio is considerably outside the range of the combined standard deviation of the calculation and the measurement (large individual chi-square).

In addition, the relative effects of using each of the two dosimeter locations individually are investigated, and the results compared with those for the optimum case. Values of the adjusted weighted fluences accumulated during cycle 9 and their reduced standard deviations at the two critical pressure vessel locations analyzed are also presented.

V.A. Adjusted Activities for the Optimum Case

A summary of the adjusted activities at both locations with their reduced standard deviations, together with the á priori values taken from Tables V, XVII, and XX, are shown in Table XXI. Note the entries in Table XXI are relative to the measurements rather than the calculations. Several observations concerning this table should be mentioned. First, the standard deviations in the dosimeter activities have been reduced by factors of approximately three by the adjustment procedure. Second, comparisons of the calculated and measured activities indicate agreement to within about one and one-and-a-half á priori combined standard deviations at the down-comer and cavity locations respectively. Third, in view of the consistent underprediction of the calculations, the adjusted activities without exception lie within about one á posteriori standard deviation of the measured values (which have the smaller uncertainties).

The covariances of the adjusted activities are shown in Table XXII. Comparison of these correlations with those before adjustment presented earlier in Table XVII indicates that, in addition to the decreases in the standard deviations effected by the adjustment procedure, the correlations are also reduced.

Table XXI. Comparison of Calculated (C) and Adjusted (A) HBR-2 Activities with Measurement (E)

	Downcomer Dosimeter		Cavity Dosimeter	
	$(C/E-1) \pm \sigma_i^a$	$(A-E)/E \pm \sigma_o$	$(C/E-1) \pm \sigma_i$	$(A-E)/E \pm \sigma_o$
$^{63}\text{Cu}(n, \alpha)^{60}\text{Co}$	$-17.3\% \pm 17.6\%$	-3.6 ± 5.1^b	-27.9 ± 23.1	-3.7 ± 7.2
$^{46}\text{Ti}(n, p)^{46}\text{Sc}$	-19.2 ± 17.5	0.6 ± 5.2	-34.5 ± 21.7	-1.1 ± 6.9
$^{54}\text{Fe}(n, p)^{54}\text{Mn}$	-17.4 ± 18.3	0.0 ± 5.4	-32.2 ± 22.6	2.8 ± 7.3
$^{58}\text{Ni}(n, p)^{58}\text{Co}$	-13.3 ± 19.2	5.5 ± 5.4	-33.9 ± 21.7	-0.3 ± 7.3
$^{238}\text{U}(n, f)^{137}\text{Cs}$	-20.0 ± 18.8	-7.1 ± 6.0	-34.8 ± 22.8	-8.7 ± 8.7
$^{237}\text{Np}(n, f)^{137}\text{Cs}$	-15.0 ± 21.4	-4.3 ± 6.4	-39.0 ± 19.4	-18.5 ± 9.4^c

^aThe values of σ_i , the relative standard deviations of (C-E), are calculated as $(\sigma_E^2 + \sigma_C^2 C^2/E^2)^{1/2}$, where σ_E and σ_C are the standard deviations of the measured and calculated activities, respectively.

^bRead as -3.6 percent with a relative standard deviation in A of 5.1 percent.

^cThis experiment was adjusted on the basis of sensitivity to the adjusted parameters only. It did not actively participate in the adjustment procedure and is included only for completeness.

Table XXII. Complete Correlation Matrix of the Adjusted Activities*

	SD (%)	Downcomer Location						Cavity Location					
		⁶³ Cu	⁴⁶ Ti	⁵⁴ Fe	⁵⁸ Ni	²³⁸ U	²³⁷ Np	⁶³ Cu	⁴⁶ Ti	⁵⁴ Fe	⁵⁸ Ni	²³⁸ U	²³⁷ Np
Downcomer Location													
⁶³ Cu	5.1	100 ^a											
⁴⁶ Ti	5.2	90	100										
⁵⁴ Fe	5.4	82	91	100									
⁵⁸ Ni	5.4	81	91	96	100								
²³⁸ U	6.0	73	74	84	87	100							
²³⁷ Np	6.4	67	68	76	79	90	100						
Cavity Location													
⁶³ Cu	7.2	73	62	54	54	50	46	100					
⁴⁶ Ti	6.9	67	76	68	67	53	49	85	100				
⁵⁴ Fe	7.3	57	67	75	72	62	55	65	87	100			
⁵⁸ Ni	7.3	56	65	71	74	66	59	64	84	97	100		
²³⁸ U	8.7	47	48	56	59	74	63	53	60	78	85	100	
²³⁷ Np	9.4	40	44	50	52	53	65	43	53	66	70	73	100

*Matrix is symmetric; only the lower half is given. The ²³⁷Np cavity dosimeter was deactivated.

^aAll elements have been multiplied by 100.

V.B. Unfolded Critical Pressure Vessel Fluxes

Summaries of the pressure vessel flux adjustments with their reduced uncertainties for several combinations of active measurements are shown in Tables XXIII and XXIV. The columns headed "none" represents the a priori standard deviations extracted from Tables XV and XVI respectively. The last four columns represent the results of the adjustment procedure when the 34 benchmark measurements are combined with (1) the six downcomer dosimeter measurements, (2) the six cavity dosimeter measurements, (3) the five cavity dosimeter measurements (the ^{237}Np reaction is excluded), and (4) the six downcomer and five cavity dosimeters simultaneously. The reductions in the standard deviations of the fluxes are seen to be less dramatic than those in the activities (or in the fluxes at the dosimeter locations), principally because there are no measurements in the pressure vessel, and the adjustments in these fluxes arise solely as a result of correlations with the calculated dosimeter activities. Comparison of the a priori column with the a posteriori column on the extreme right (the most consistent combination) in each table shows the standard deviations are reduced by factors of between 1.2 and 2. Except for the two highest energy groups, significant flux adjustments occur throughout the spectrum at both critical pressure vessel locations, particularly in the energy range from 3 to 8 MeV, perhaps severely testing the linearity assumption implicit in the LEPRICON procedure over this limited energy region.

The question as to which dosimeter location provides more information regarding the flux levels in the pressure vessel is also quantitatively answered by inspection of Tables XXIII and XXIV. The downcomer dosimetry underestimates the magnitudes of the flux adjustments compared with those from the most consistent combination of measurements, whereas the cavity dosimetry using five dosimeters produces results much closer to those obtained from combining data at both locations simultaneously. Thus the conclusion is inescapable that the cavity dosimetry location possesses the higher weight in the combining process, at least compared with the off-azimuth downcomer location employed in this analysis. There are still some advantages to using downcomer dosimetry, of course, if it can be positioned in close proximity to the critical pressure vessel location. Under these conditions it should provide accurate adjustments of all the parameters that originally affect the pressure vessel flux, but at the expense of introducing other uncertainties which involve partial shielding effects of the surveillance capsule on local pressure vessel flux levels that are less readily reduced in an adjustment procedure. The ideal situation, from the standpoint of monitoring flux levels at several pressure vessel locations simultaneously, is to combine the use of a surveillance capsule containing both metallurgical specimens and dosimetry at a downcomer position adjacent to the PTS-critical weld location in the pressure vessel with ex-vessel cavity dosimetry positioned near the azimuth of maximum flux.

The autocorrelation matrix of the unfolded critical pressure vessel fluxes at the LCW location appears in Table XXV. The corresponding matrix for the fluxes at the critical T/4 location is quite similar, differing significantly only in the columns assigned to the first two groups where

Table XXIII. Flux Adjustments and Standard Deviations at the Critical LCW Pressure Vessel Location as Functions of HBR-2 Measurements Activated

Flux Group	Lower Energy (MeV)	None	34 Benchmarks +			
			6 Downcomer Only	6 Cavity Only	5 Cavity Only	6 Downcomer + 5 Cavity
1	11.1	0 ± 20.6 ^a	-0.5 ± 12.5	4.5 ± 11.2	5.7 ± 11.3	8.2 ± 11.0
2	8.2	0 ± 19.0	-3.5 ± 12.4	2.1 ± 10.9	3.3 ± 10.9	6.3 ± 10.5
3	6.1	0 ± 17.8	22.9 ± 12.1	26.7 ± 10.8	27.5 ± 10.8	29.9 ± 10.3
4	4.1	0 ± 18.2	25.3 ± 12.9	29.0 ± 11.4	29.5 ± 11.4	32.0 ± 10.8
5	3.0	0 ± 18.1	23.2 ± 13.5	27.3 ± 12.1	27.4 ± 12.1	30.1 ± 11.5
6	2.6	0 ± 16.5	12.2 ± 13.8	15.5 ± 12.4	16.7 ± 12.4	20.3 ± 11.3
7	2.1	0 ± 16.5	9.2 ± 14.2	12.4 ± 12.7	13.9 ± 12.7	17.9 ± 12.1
8	1.8	0 ± 16.5	9.9 ± 14.1	13.5 ± 12.7	14.6 ± 12.7	18.4 ± 12.2
9	1.5	0 ± 16.5	9.7 ± 14.2	13.5 ± 12.9	14.6 ± 12.9	18.4 ± 12.3
10	1.2	0 ± 16.5	9.6 ± 14.3	13.8 ± 12.9	14.5 ± 12.9	18.3 ± 12.3
11	0.9	0 ± 16.2	10.4 ± 14.1	15.0 ± 12.8	15.2 ± 12.8	18.7 ± 12.3
12	0.6	0 ± 15.5	11.4 ± 13.9	19.0 ± 12.8	15.5 ± 12.9	18.2 ± 12.5
13	0.4	0 ± 15.7	11.5 ± 14.1	18.8 ± 13.0	15.5 ± 13.1	18.3 ± 12.7
14	0.2	0 ± 15.6	11.6 ± 14.0	18.5 ± 13.0	15.7 ± 13.0	18.5 ± 12.7
15	0.1	0 ± 15.7	11.4 ± 14.1	18.2 ± 13.0	15.5 ± 13.1	18.5 ± 12.7

^aRead as a change of 0 percent with a standard deviation of 20.6 percent.

Table XXIV. Flux Adjustments and Standard Deviations at the Critical T/4 Pressure Vessel Location as Functions of the HBR-2 Measurements Activated

Flux Group	Lower Energy (MeV)	None	34 Benchmarks +			
			6 Downcomer Only	6 Cavity Only	5 Cavity Only	6 Downcomer + 5 Cavity
1	11.1	0 ± 22.9 ^a	-4.6 ± 13.0	0.4 ± 11.2	3.1 ± 11.3	6.1 ± 10.9
2	8.2	0 ± 21.7	-7.8 ± 13.0	-2.3 ± 10.8	0.5 ± 10.9	3.9 ± 10.4
3	6.1	0 ± 20.4	29.5 ± 12.2	32.5 ± 10.3	34.7 ± 10.4	37.2 ± 9.7
4	4.1	0 ± 21.3	33.4 ± 13.1	36.2 ± 11.1	38.0 ± 11.2	40.6 ± 10.4
5	3.0	0 ± 20.7	30.5 ± 13.6	33.9 ± 11.7	35.2 ± 11.8	37.9 ± 11.0
6	2.6	0 ± 17.8	15.4 ± 13.8	17.4 ± 11.9	20.3 ± 12.0	24.3 ± 11.2
7	2.1	0 ± 17.7	11.3 ± 14.2	13.1 ± 12.3	16.5 ± 12.4	20.8 ± 11.6
8	1.8	0 ± 17.5	12.3 ± 14.0	14.5 ± 12.2	17.4 ± 12.3	21.5 ± 11.6
9	1.5	0 ± 17.4	12.0 ± 14.1	14.6 ± 12.3	17.3 ± 12.4	21.5 ± 11.7
10	1.2	0 ± 17.5	11.8 ± 14.2	14.9 ± 12.4	17.2 ± 12.5	21.4 ± 11.7
11	0.9	0 ± 16.9	12.9 ± 13.8	17.6 ± 12.2	18.1 ± 12.2	21.9 ± 11.5
12	0.6	0 ± 15.4	14.4 ± 13.2	21.5 ± 11.9	18.5 ± 12.0	21.4 ± 11.6
13	0.4	0 ± 15.6	14.4 ± 13.4	21.3 ± 12.1	18.6 ± 12.2	21.5 ± 11.8
14	0.2	0 ± 15.6	14.6 ± 13.3	21.1 ± 12.1	18.8 ± 12.2	21.7 ± 11.7
15	0.1	0 ± 15.6	14.4 ± 13.4	20.8 ± 12.2	18.6 ± 12.3	21.6 ± 11.8

^aRead as a change of 0 percent with a standard deviation of 22.9 percent.

Table XXV. Autocorrelation Matrix of the Adjusted Group Fluxes at the Critical LCW Pressure Vessel Location*

Flux Group	Lower Energy (MeV)	SD (%)	1	2	3	4	5	6	7	8	9	10	11	12	13	14	15
1	11.1	11.0	100 ^a														
2	8.2	10.5	83	100													
3	6.1	10.3	67	68	100												
4	4.1	10.8	62	64	85	100											
5	3.0	11.5	63	66	84	85	100										
6	2.6	11.8	68	72	79	79	81	100									
7	2.1	12.1	68	72	77	77	79	85	100								
8	1.8	12.2	68	72	78	78	80	85	85	100							
9	1.5	12.3	68	72	78	78	80	85	85	85	100						
10	1.2	12.3	68	72	78	78	80	85	85	85	85	100					
11	0.9	12.3	67	71	78	79	81	83	83	84	84	85	100				
12	0.6	18.5	64	69	78	79	82	81	80	81	82	82	83	100			
13	0.4	18.6	64	68	77	79	81	81	80	81	81	81	83	85	100		
14	0.2	18.7	63	68	77	78	81	80	80	81	81	81	83	85	85	100	
15	0.1	18.7	63	68	77	78	81	80	79	80	81	81	83	84	85	85	100

*Matrix is symmetric; only the lower half is shown.

^aAll elements have been multiplied by 100.

the flux correlations at T/4 average about 20 percent lower. The general pattern observed in previous adjustments^{2,3} that the pressure vessel flux correlations decrease upon adjustment remains true for HBR-2, but there are a few exceptions as can be seen by comparing Tables XXV and XV. The changes, however, are relatively small. As an illustration of a case in which the autocorrelations decrease more dramatically upon adjustment, Table XXVI presents the a posteriori autocorrelation matrix of the group fluxes at the cavity dosimetry location, where they may be compared with the a priori values previously presented in Table XIV.

V.C. Adjustments in the Parameters

In agreement with the results of the previous ANO-1 adjustments,³ significant changes are again observed in the high-energy region of the fission spectrum from ^{235}U , varying between increases of 4 and 8 percent for the groups above 6 MeV. As has been observed consistently throughout all previous applications of the LEPRICON adjustment procedure with its ENDF/B-V data base,^{2,3} the most significant change in any of the parameters is found in the total inelastic iron cross section in the region from 3 to 8 MeV. The results of the present analysis along with those of the earlier analyses are summarized in Table XXVII for the this energy region. It can be seen that the adjustments based on a simultaneous combination of the benchmark measurements with the 11 HBR-2 measurements remain quite consistent with those based on a simultaneous combination of the same benchmarks with the ANO-1 measurements, as well as with those based on activating only the benchmarks themselves.

Even though relatively large uncertainties are attributed to the flux bias factors arising from the uncertainty in the downcomer dosimeter location, adjustments in these bias factors were virtually negligible, thus establishing that a consistent adjustment using both dosimeter locations was possible without invoking this particular source of uncertainty. The large uncertainties in this bias factor that are part of the LEPRICON data base were based on the consideration of possible long-term capsule displacement effects caused by possibly violent coolant conditions at times in the downcomer. Since the dummy downcomer capsule in the present analysis was inserted only for cycle 9, the period of time it was subjected to coolant buffeting was considerably less than that of a typical capsule and as a consequence it is indeed very likely that its position remained close to that of its original placement during the entire cycle 9 exposure.

The only flux bias factors that were in any significant way changed as a result of the adjustment procedure are those arising from the pressure vessel out-of-roundness. Details of these parameter adjustments are summarized in Table XXVIII for the cavity dosimeter and pressure vessel locations. The a priori standard deviations appearing in this table are extracted from Tables XI and XII respectively. Since the uncertainties in the pressure vessel fluxes at both the critical LCW and T/4 locations arising from this bias factor are virtually the same and the cross correlations between the cavity location and either pressure vessel location are

Table XXVI. Autocorrelation Matrix of the Adjusted Group Fluxes at the Cavity Dosimetry Location*

Flux Group	Lower Energy (MeV)	SD (%)	1	2	3	4	5	6	7	8	9	10	11	12	13	14	15
1	11.1	14.6	100 ^a														
2	8.2	13.7	81	100													
3	6.1	11.2	9	4	100												
4	4.1	12.4	-4	-10	88	100											
5	3.0	12.1	2	-4	87	88	100										
6	2.6	11.6	26	24	60	57	60	100									
7	2.1	12.5	31	29	49	45	48	86	100								
8	1.8	12.1	30	28	53	49	53	87	88	100							
9	1.5	11.9	31	28	53	50	54	86	87	87	100						
10	1.2	12.0	32	29	54	50	56	84	85	86	86	100					
11	0.9	11.3	29	25	58	56	63	75	73	76	78	82	100				
12	0.6	10.2	12	10	56	59	64	53	48	52	55	56	64	100			
13	0.4	10.5	12	11	55	58	63	53	48	52	55	56	65	83	100		
14	0.2	10.6	12	11	55	58	63	53	47	52	55	56	65	83	83	100	
15	0.1	10.6	11	10	54	56	62	52	47	51	54	55	64	82	83	83	100

*Matrix is symmetric; only the lower half is shown.

^aAll elements have been multiplied by 100.

Table XXVII. Summary of Present and Past Adjustments in the Total Inelastic Cross Section of Iron in the 3- to 8-MeV Region

Energy Group	Energy Range (MeV)	ENDF/B ^a	PCA	+	PSF	+	ANO-1	or	HBR-2 ^b
3	6.1 - 8.2	0.0 ± 5.4 ^c	-8.9 ± 3.7		-8.7 ± 2.7		-8.2 ± 2.2		-9.4 ± 2.2
4	4.1 - 6.1	0.0 ± 5.5	-9.0 ± 3.7		-9.2 ± 2.7		-8.6 ± 2.2		-9.7 ± 2.2
5	3.0 - 4.1	0.0 ± 5.6	-8.9 ± 3.9		-9.0 ± 2.8		-8.5 ± 2.3		-9.7 ± 2.3

^aThe a priori values were taken from ENDF/B-V.

^bThe HBR-2 results include approximate contributions from chromium and nickel as well.

^cRead as an adjustment of 0 percent with a standard deviation of 5.4 percent.

Table XXVIII. Adjustments and Standard Deviations in the Pressure Vessel Out-of-Roundness Bias Factor at the Cavity Dosimeter and Critical Pressure Vessel Locations

Flux Group	Lower Energy (MeV)	Cavity Location			Pressure Vessel Location ^a		
		Change (%)	Standard Deviation (%)		Change (%)	Standard Deviation (%)	
			Old	New		Old	New
1	11.1	5.0	6.7	5.5	4.6	6.8	5.8
2	8.2	5.7	7.3	5.9	5.2	7.4	6.3
3	6.1	6.2	7.9	6.4	5.6	7.9	6.6
4	4.1	6.4	8.6	6.9	5.9	8.6	7.2
5	3.0	6.7	9.2	7.5	6.1	9.5	8.1
6	2.6	7.1	9.6	7.8	6.4	10.0	8.6
7	2.1	7.4	9.9	8.0	6.7	10.2	8.7
8	1.8	7.4	9.9	8.1	6.8	10.3	8.8
9	1.5	7.7	10.1	8.2	7.0	10.5	9.0
10	1.2	7.7	10.2	8.3	7.0	10.6	9.1
11	0.9	7.8	10.3	8.4	7.1	10.6	9.1
12	0.6	7.9	10.5	8.6	7.2	10.9	9.4
13	0.4	7.9	10.6	8.6	7.2	10.9	9.3
14	0.2	8.0	10.7	8.7	7.3	10.9	9.3
15	0.1	8.0	10.7	8.7	7.3	10.9	9.3

^aResults are the same for both the critical LCW and T/4 locations.

also assumed to be the same (see Table IX), the adjustments at both pressure vessel locations are identical and are due to an inferred decrease in the downcomer thickness of about 6 mm (0.24 in.) from its nominal value.

V.D. Adjusted Critical Pressure Vessel Fluences

Values of the adjusted group fluences accumulated during cycle 9 at each of the two pressure vessel locations may be readily obtained by multiplying the entries in Table VIII by the adjustment factors appearing in the last columns of Tables XXIII and XXIV. These adjusted fluences appear in Table XXIX. Values of three weighted pressure vessel fluences for both the calculated and adjusted cases are shown in Table XXX. The adjusted values are seen to average ~15 percent higher than the originally calculated values for either pressure vessel location and the standard deviations have been reduced from about 16 to 11 percent.

Table XXIX. Adjusted Group Fluences at the Critical Pressure Vessel Locations Accumulated During Cycle 9

Group	Lower Energy (MeV)	Fluence in $n \cdot \text{cm}^{-2}$		Group	Lower Energy (MeV)	Fluence in $n \cdot \text{cm}^{-2}$	
		LCW	T/4			LCW	T/4
1	14.2	$1.29 + 14^a$	$4.94 + 13$	20	2.12	$2.84 + 16$	$1.44 + 16$
2	12.2	$6.38 + 14$	$2.51 + 14$	21	1.92	$5.36 + 16$	$2.73 + 16$
3	11.1	$8.22 + 14$	$3.19 + 14$	22	1.83	$2.72 + 16$	$1.57 + 16$
4	10.0	$1.82 + 15$	$6.96 + 14$	23	1.65	$6.43 + 16$	$3.80 + 16$
5	8.61	$5.37 + 15$	$2.03 + 15$	24	1.50	$6.07 + 16$	$3.60 + 16$
6	8.19	$2.51 + 15$	$9.41 + 14$	25	1.35	$6.74 + 16$	$4.39 + 16$
7	7.41	$8.52 + 15$	$3.35 + 15$	26	1.23	$6.34 + 16$	$4.25 + 16$
8	7.05	$4.78 + 15$	$1.89 + 15$	27	1.00	$1.38 + 17$	$1.08 + 17$
9	6.07	$2.31 + 16$	$8.71 + 15$	28	0.907	$6.45 + 16$	$5.77 + 16$
10	4.97	$4.00 + 16$	$1.46 + 16$	29	0.821	$7.01 + 16$	$5.82 + 16$
11	4.07	$4.98 + 16$	$1.81 + 16$	30	0.743	$7.16 + 16$	$5.22 + 16$
12	3.68	$2.33 + 16$	$8.81 + 15$	31	0.608	$2.06 + 17$	$2.32 + 17$
13	3.01	$5.76 + 16$	$2.30 + 16$	32	0.498	$1.62 + 17$	$1.62 + 17$
14	2.73	$4.19 + 16$	$1.77 + 16$	33	0.369	$2.04 + 17$	$2.36 + 17$
15	2.59	$2.44 + 16$	$1.10 + 16$	34	0.302	$1.7 + 17$	$2.20 + 17$
16	2.47	$2.40 + 16$	$1.02 + 16$	35	0.213	$2.03 + 17$	$2.14 + 17$
17	2.37	$2.45 + 16$	$1.08 + 16$	36	0.183	$7.26 + 16$	$7.25 + 16$
18	2.35	$7.00 + 15$	$3.33 + 15$	37	0.111	$2.29 + 17$	$2.33 + 17$
19	2.23	$3.26 + 16$	$1.63 + 16$	38	0.098	$4.09 + 16$	$3.70 + 16$

^aRead as 1.29×10^{14} .

Table XXX. Weighted Fluences at the Critical Pressure Vessel Locations Accumulated During Cycle 9 with Standard Deviations Before and After Unfolding

	LCW Location		T/4 Location	
	Before	After	Before	After
Fluence above 1.00 MeV	7.23(17) ± 1.15(17) ^a	8.37(17) ± 0.91(17)	3.86(17) ± 0.66(17)	4.43(17) ± 0.47(17)
Fluence above 0.098 MeV	1.99(18) ± 0.30(18)	2.26(18) ± 0.26(18)	1.68(18) ± 0.26(18)	1.90(18) ± 0.20(18)
dpa above 0.098 MeV	1.11(-3) ± 0.17(-3) ^b	1.28(-3) ± 0.14(-3)	7.16(-4) ± 1.13(-4)	8.18(-4) ± 0.85(-4)

^aRead as $7.23 \times 10^{17} \pm 1.15 \times 10^{17} \text{ n/cm}^2$.

^bRead as $1.11 \times 10^{-3} \pm 0.17 \times 10^{-3}$ displacements per atom of iron.

VI. SUMMARY AND CONCLUSIONS

It has been demonstrated that the LEPRICON computer code system, as it now exists, can be successfully applied to the analysis of surveillance dosimetry recently installed in an older Westinghouse three-loop reactor. Since the reactor design as well as in-core instrumentation analysis procedures for the HBR-2 and ANO-1 reactors are different, it is comforting to know that the code system is sufficiently general to be able to treat geometries of considerable diversity, as well as being capable of taking advantage of core-follow analysis routinely performed by different vendors such as Westinghouse and Babcock and Wilcox.

At the beginning of the present analysis, it was felt that the presence of the relatively narrow reactor cavity in HBR-2 might introduce calculational problems that were absent in the wide cavity of ANO-1. Such was not the case, however, either because the cavity was not so narrow as to cause a streaming problem over the range of heights investigated, the presence of two deep and wide detector wells effectively widened the cavity, or the core source distribution was flat over much of the axial range analyzed, or perhaps a combination of all three. For whatever reason, no progress could be made on refining the knowledge of the bias factor arising from streaming effects on off-midplane dosimetry locations in narrow cavities that is included as a parameter in the LEPRICON system and which could still apply to certain other reactors.

The considerably off-midplane location of the lower circumferential weld was also somewhat of a preanalysis worry, since the axial range of validity of the three-dimensional flux synthesis procedure was not severely tested in ANO-1. Fortunately, in HBR-2 the axial flatness of the source beyond this point ensured the success of the procedure.

There still exist reactors, however, for which a priori values for the flux synthesis bias factors are not unity, i.e., reactors in which the locations of the critical PTS-sensitive welds fall beyond the range of validity of the simple synthesis procedure. Such axial locations occur in regions of large vertical flux gradients occasioned by proximity to the limits of the active core and beyond. Evaluation of these bias factors still needs to be performed before the LEPRICON procedure can be applied indiscriminately to end-of-life and PTS pressure vessel locations alike.

The results of the present analysis are similar to those from ANO-1. Meaningful reductions in the estimated standard deviations of the pressure vessel fluences accumulated during cycle 9 from 16 to 11 percent were obtained for both locations, with the adjusted fluences being about 15 percent higher. By eliminating one of the 12 measurements, the HBR-2 data were found to be consistent with previously analyzed benchmark data that form an important part of the data base developed for the adjustment procedure.

Of the two dosimetry locations simultaneously employed in HBR-2, those in the cavity offer more information on the pressure vessel fluxes because they have about the same sensitivity to any pressure vessel out-of-roundness as either critical pressure vessel location; they also possess high sensitivity to inaccuracies in the steel transport cross sections which also affect the pressure vessel fluxes.

ADDENDUM

Since 1981, it has been generally accepted by the U.S. dosimetry community that iron cross section sets derived from ENDF/B-IV and ENDF/B-V evaluations were somewhat deficient because of the relatively poor agreement between calculations using these sets and measurements of dosimeter activities in various benchmark mockups involving penetration through different thicknesses of simulated pressure vessels. It has been further conjectured that the deficiency lay principally in the treatment of the inelastic cross section, since this is the primary mechanism in the MeV region whereby neutrons may lose considerable amounts of energy. Too large a cross section would result in underprediction of the neutron fluxes that contribute heavily to the threshold dosimeter reaction rates such as those described in this report. From the viewpoint of the LEPRICON analysis, the consistent underpredictions of the measured activities in the benchmark experiments, the ANO-1 reactor, and now the HBR-2 reactor are explainable in terms of an inelastic cross section that is about 8 to 9 percent too high in the energy range of 3 to 8 MeV (see Table XXVII). The uncertainties in this cross section in this particular energy range are described in ENDF/B-V as being fully correlated, which is also somewhat unrealistic.

At least two new iron evaluations have appeared in 1986, one by Los Alamos and the other by Oak Ridge. Both involve changes in the description of the inelastic scattering, and the Oak Ridge version in addition includes an updated contribution from ^{57}Fe so that its evaluation is representative of natural iron. Compared with ENDF/B-V, the new Oak Ridge evaluation has about a ~10 percent smaller total inelastic cross section in the range above 4 MeV and a forward-peaked (compared with isotropic for ENDF/B-V) angular distribution of the inelastically scattered neutrons, both of which would result in less attenuation by the revised evaluation to MeV neutrons.

We have collapsed the VITAMIN-E version of this new Oak Ridge evaluation to the ELXSIR group structure and repeated the $R-\theta$ reference transport calculation described earlier in this report, so that comparisons could be made between the results using the revised and original libraries. These comparisons are summarized in Table XXXI.

With the exception of the $^{237}\text{Np}(n,f)$ dosimeter in the cavity, a noticeable improvement in the agreement is shown using the new cross sections, and they are strongly recommended for future calculations.

Table XXXI. Comparisons with Measurement of Calculated
End-of-Cycle Activities Using Original
and Updated Iron Cross Sections

At 20-deg Downcomer Location		
Dosimeter	(C/E) original	(C/E) updated
$^{63}\text{Cu}(n, \alpha)^{60}\text{Co}$	0.83	1.01
$^{46}\text{Ti}(n, p)^{46}\text{Sc}$	0.81	1.00
$^{54}\text{Fe}(n, p)^{54}\text{Mn}$	0.83	0.99
$^{58}\text{Ni}(n, p)^{58}\text{Co}$	0.87	1.03
$^{238}\text{U}(n, f)^{137}\text{Cs}$	0.80	0.91
$^{237}\text{Np}(n, f)^{137}\text{Cs}$	0.85	0.93
At 0-deg Cavity Location		
Dosimeter	(C/E) original	(C/E) updated
$^{63}\text{Cu}(n, \alpha)^{60}\text{Co}$	0.72	1.17
$^{46}\text{Ti}(n, p)^{46}\text{Sc}$	0.66	1.11
$^{54}\text{Fe}(n, p)^{54}\text{Mn}$	0.68	1.07
$^{58}\text{Ni}(n, p)^{58}\text{Co}$	0.66	1.00
$^{238}\text{U}(n, f)^{137}\text{Cs}$	0.65	0.83
$^{237}\text{Np}(n, f)^{137}\text{Cs}$	0.61	0.60

ACKNOWLEDGMENTS

The author wishes to express his sincere appreciation to W. K. Cantrell of CP&L for promptly providing all the necessary information on HBR-2 cycle 9 reactor performance. He is equally grateful to E. P. Lippincott and S. L. Anderson of Westinghouse for providing details of the reactor geometry as well as the end-of-cycle dosimeter activities with estimates of their uncertainties. The cooperation of Sam Grant of CP&L is also gratefully acknowledged. The author is indebted to B. L. Broadhead of Oak Ridge National Laboratory (ORNL) for providing working versions of the LEPRICON code system and for his invaluable assistance during the course of this work. Thanks are also due F. B. K. Kam of ORNL and C. Z. Serpan of the NRC for their financial support and encouragement, and O. Ozer of EPRI for persuading EPRI to share the LEPRICON code system with NRC. Finally, we wish to acknowledge the work of Karen Harber in the preparation of this manuscript.

NUREG/CR-4439
 ORNL/TM-10132
 Dist. Category RL

INTERNAL DISTRIBUTION

- | | |
|------------------------------------|----------------------------------|
| 1. C. A. Baldwin | 24. E. Newman |
| 2. B. L. Broadhead | 25. F. G. Pin |
| 3. C. D. Cagle | 26. F. W. Stallmann |
| 4. P. W. Dickson, Jr. (Consultant) | 27. D. Steiner (Consultant) |
| 5. D. M. Eissenberg | 28. J. H. Swanks |
| 6. G. H. Golub (Consultant) | 29. B. J. Taylor |
| 7. R. M. Haralick (Consultant) | 30. C. R. Weisbin |
| 8-9. J. K. Ingersoll | 31. A. Zucker |
| 10-14. F. B. K. Kam | 32. Document Reference Section |
| 15-19. R. E. Maerker | 33. Central Research Library |
| 20. F. C. Maienschein | 34. Laboratory Records Dept. |
| 21. A. P. Malinauskas | 35. Laboratory Records-ORNL R.C. |
| 22. L. F. Miller | 36. ORNL Patent Office |
| 23. F. R. Mynatt | |

EXTERNAL DISTRIBUTION

37. Lambros Lois, U.S. Nuclear Regulatory Commission, Phillips Building, Mail Stop P-924, Washington, DC 20555
38. M. L. Williams, Nuclear Science Center, Louisiana State University, Baton Rouge, LA 70803-5820
39. C. Z. Serpan, Jr., Division of Engineering Technology, Nuclear Regulatory Commission, Mail Stop SS-1130, Washington, DC 20555
40. M. Vagins, Division of Engineering Technology, Nuclear Regulatory Commission, Washington, DC 20555
41. A. Taboada, Nuclear Regulatory Commission, Mail Code NL 5650, Washington, DC 20555
42. O. Ozer, Nuclear Power Division, Electric Power Research Institute, P.O. Box 10412, Palo Alto, CA 94303
- 43-45. S. P. Grant, Carolina Power & Light Co., P.O. Box 1551, Raleigh, NC 27602
46. Assistant Manager for Energy Research and Development, U.S. Department of Energy, Oak Ridge Operations Office, P.O. Box E., Oak Ridge, TN 37831
- 47-48. Technical Information Center, U.S. Department of Energy, Office of Information Services, P.O. Box 62, Oak Ridge, TN 37831
- 49-223. Given distribution under category RL (10 copies - NTIS)

BIBLIOGRAPHIC DATA SHEET

NUREG/CR-4439
ORNL/TM-10132

SEE INSTRUCTIONS ON THE REVERSE

2 TITLE AND SUBTITLE

LEPRICON Analysis of Pressure Vessel Surveillance
Dosimetry Inserted into H. B. Robinson-2 During
Cycle 9

3 LEAVE BLANK

4 DATE REPORT COMPLETED

MONTH

July

YEAR

1986

5 AUTHOR(S)

R. E. Maerker

6 DATE REPORT ISSUED

MONTH

September

YEAR

1986

7 PERFORMING ORGANIZATION NAME AND MAILING ADDRESS (Include Zip Code)

Engineering Physics and Mathematics Division
Oak Ridge National Laboratory
P.O. Box X
Oak Ridge, TN 37831

8 PROJECT TASK WORK UNIT NUMBER

9 FIN OR GRANT NUMBER

B0415

10 SPONSORING ORGANIZATION NAME AND MAILING ADDRESS (Include Zip Code)

U.S. Nuclear Regulatory Commission
Washington, DC 20555

11a TYPE OF REPORT

Topical

b PERIOD COVERED (Inclusive dates)

January - July 1986

12 SUPPLEMENTARY NOTES

13 ABSTRACT (200 words or less)

ABSTRACT

A second example of applying the LEPRICON methodology to an existing pressurized water reactor is described. The present application is an analysis of *ad hoc* dosimetry inserted into the H. B. Robinson-2 reactor to monitor the effects on pressure vessel fluence produced by the introduction of a low-leakage fuel management scheme during cycle 9. The use of simultaneous dosimetry both at a downcomer location and in the reactor cavity allowed a quantitative evaluation to be made by the LEPRICON procedure of the relative merits of each location. Unfolded results using the dosimetry indicate that the cumulative neutron fluence above 1 MeV originally calculated for the critical lower circumferential weld in the pressure vessel during cycle 9, $7.2 \times 10^{17} \text{n/cm}^2 \pm 15.9$ percent, should be adjusted upward by about one standard deviation to a value of $8.4 \times 10^{17} \text{n/cm}^2$ with a reduced uncertainty of 10.9 percent.

14 DOCUMENT ANALYSIS -- KEYWORDS/DESCRIPTORS

15 IDENTIFIERS OPEN ENDED TERMS

16 AVAILABILITY STATEMENT

Unlimited

16 SECURITY CLASSIFICATION

(This page)

Unclassified

(This report)

Unclassified

17 NUMBER OF PAGES

69

18 PRICE

120555078877 1 1A1RL
US NRC
ADM-DIV OF TIDC
POLICY & PUB MGT BR-PDR NUREG
W-501 DC 20555
WASHINGTON